ANL/RTR/TM-15/2

Thermal-Hydraulic Simulations of Single Pin and Assembly Sector for IVG-1M Reactor

Nuclear Engineering Division

About Argonne National Laboratory
Argonne is a U.S. Department of Energy laboratory managed by UChicago Argonne, LLC under contract DE-AC02-06CH11357. The Laboratory's main facility is outside Chicago, at 9700 South Cass Avenue, Argonne, Illinois 60439. For information about Argonne and its pioneering science and technology programs, see www.anl.gov.

DOCUMENT AVAILABILITY

Online Access: U.S. Department of Energy (DOE) reports produced after 1991 and a growing number of pre-1991 documents are available free via DOE's SciTech Connect (http://www.osti.gov/scitech/)

Reports not in digital format may be purchased by the public from the National Technical Information Service (NTIS):
U.S. Department of Commerce National
Technical Information Service 5301
Shawnee Rd
Alexandria, VA 22312
www.ntis.gov
Phone: (800) 553-NTIS (6847) or (703) 605-6000
Fax: (703) 605-6900
Email: **orders@ntis.gov**

Reports not in digital format are available to DOE and DOE contractors from the Office of Scientific and Technical Information (OSTI):
U.S. Department of Energy
Office of Scientific and Technical Information
P.O. Box 62
Oak Ridge, TN 37831-0062
www.osti.gov
Phone: (865) 576-8401
Fax: (865) 576-5728
Email: **reports@osti.gov**

Disclaimer
This report was prepared as an account of work sponsored by an agency of the United States Government. Neither the United States Government nor any agency thereof, nor UChicago Argonne, LLC, nor any of their employees or officers, makes any warranty, express or implied, or assumes any legal liability or responsibility for the accuracy, completeness, or usefulness of any information, apparatus, product, or process disclosed, or represents that its use would not infringe privately owned rights. Reference herein to any specific commercial product, process, or service by trade name, trademark, manufacturer, or otherwise, does not necessarily constitute or imply its endorsement, recommendation, or favoring by the United States Government or any agency thereof. The views and opinions of document authors expressed herein do not necessarily state or reflect those of the United States Government or any agency thereof, Argonne National Laboratory, or UChicago Argonne, LLC.

ANL/RTR/TM-15/2

Thermal-Hydraulic Simulations of Single Pin and Assembly Sector for IVG-1M Reactor

prepared by

A. Kraus, P. Garner and N. Hanan
Nuclear Engineering Division
Argonne National Laboratory

1/15/2015

Table of Contents

I. SUMMARY 6
II. INTRODUCTION 7
III. STEADY-STATE SIMULATIONS 12
A. Methods 12
i. 600 mm Assembly 13
ii. 800 mm Assembly (HEU Design) 17
B. Single-Pin Results 18
i. 600 mm 18
ii. 800 mm 26
C. Assembly Results 27
i. 600 mm 27
ii. 800 mm 36
IV. TRANSIENT SIMULATIONS 37
A. Methods 37
B. Results 40
i. “Ramp” Transient 40
ii. “Step” Transient 42
V. CONCLUSIONS 48
VI. ACKNOWLEDGMENTS 48
VII. REFERENCES 48

I. SUMMARY

Thermal-hydraulic simulations have been performed using computational fluid dynamics (CFD) for the highly-enriched uranium (HEU) design of the IVG.1M reactor at the Institute of Atomic Energy (IAE) at the National Nuclear Center (NNC) in the Republic of Kazakhstan. Steady-state simulations were performed for both types of fuel assembly (FA), i.e. the FA in rows 1 & 2 and the FA in row 3, as well as for single pins in those FA (600 mm and 800 mm pins). Both single pin calculations and bundle sectors have been simulated for the most conservative operating conditions corresponding to the 10 MW output power, which corresponds to a pin unit cell Reynolds number of only about 7500. Simulations were performed using the commercial code STAR-CCM+ for the actual twisted pin geometry as well as a straight-pin approximation. Various Reynolds-Averaged Navier-Stokes (RANS) turbulence models gave different results, and so some validation runs with a higher-fidelity Large Eddy Simulation (LES) code were performed given the lack of experimental data. These singled out the Realizable Two-Layer k-ε as the most accurate turbulence model for estimating surface temperature.

Single-pin results for the twisted case, based on the average flow rate per pin and peak pin power, were conservative for peak clad surface temperature compared to the bundle results. Also the straight-pin calculations were conservative as compared to the twisted pin simulations, as expected, but the single-pin straight case was not always conservative with regard to the straight-pin bundle. This was due to the straight-pin temperature distribution being strongly influenced by the pin orientation, particularly near the outer boundary. The straight-pin case also predicted the peak temperature to be in a different location than the twisted-pin case. This is a limitation of the straight-pin approach.

The peak temperature pin was in a different location from the peak power pin in every case simulated, and occurred at an inner pin just before the enrichment change. The 600 mm case demonstrated a peak clad surface temperature of 370.4 K, while the 800 mm case had a temperature of 391.6 K. These temperatures are well below the necessary temperatures for boiling to occur at the rated pressure. Fuel temperatures are also well below the melting point. Future bundle work will include simulations of the proposed low-enriched uranium (LEU) design.

Two transient scenarios were also investigated for the single-pin geometries. Both were “model” problems that were focused on pure thermal-hydraulic behavior, and as such were simple power changes that did not incorporate neutron kinetics modeling. The first scenario was a high-power, ramp increase, while the second scenario was a low-power, step increase. A cylindrical RELAP model was also constructed to investigate its accuracy as compared to the higher-fidelity CFD. Comparisons between the two codes showed good agreement for peak temperatures in the fuel and at the cladding surface for both cases. In the step transient, temperatures at four axial levels were also computed. These showed greater but reasonable discrepancy, with RELAP outputting

higher temperatures. These results provide some evidence that RELAP can be used with confidence in modeling transients for IVG.

II. INTRODUCTION

The geometries and flow conditions found in nuclear research reactors can present modeling and simulation challenges. The DOE/NNSA Reactor Conversion Program is tasked with investigating and applying analysis methods for research reactors. The overall goal is to convert reactors from HEU to LEU fuel to reduce proliferation concerns while striving to maintain the unique characteristics of each reactor, such as high neutron flux in a given area. Generally the HEU design must first be confidently modeled to ensure that the physical behavior of the reactor is well understood. This allows for establishment of appropriate analysis methods and generally also leads to a more sound LEU design.

The IVG.1M reactor at the NNC in Kazakhstan is one such reactor with exotic geometry. The design of the FAs and fuel elements (FEs) is described in detail in the Deliverable 2.1 report (Ref. 1) and only a short description is provided here. The core features annular assemblies containing twisted fuel pins in a roughly hexagonal lattice, which can be seen in Fig. 1-Fig. 3. There are two zones featuring different enrichments in each FA. The pins are in direct contact with one another and with the assembly can walls. There are cylindrical filler rods, made of E-110 Zr-Nb alloy, to maintain appropriate spacing given the circular inner and outer assembly boundaries. Some specifications for the fuel pins are provided in

Table 1. The fuel is a U-Zr alloy and the cladding is E-110 alloy. Both fuel and clad are twisted together. The top and bottom ends of the pin are assumed to be comprised of 1 mm of only cladding.

There are two different assembly types. One has 600 mm-length pins (termed the “600 mm” bundle), while the other has similar 600 mm pins but also 200 mm pins stacked above them (the “800 mm” bundle) which are separated from them by a metal grid and mesh screen (Fig. 4-Fig. 5). High-fidelity analysis was performed for the peak power assemblies for both FA types, based on a possible configuration used for the IVG.1M reactor. With the exception of the grid, there are no obstructions of the flow path for the entire fuel length of either FA. For the 600 mm pins, the assembly center is 7.4 mm in diameter; for the 200 mm pins, the center is 12 mm in diameter (Fig. 5). For this reason, there are 468 pins of the 600 mm variety and 456 pins of the 200 mm variety. The 200 mm pin layout is identical to the 600 mm layout except without the center-most 12 pins.

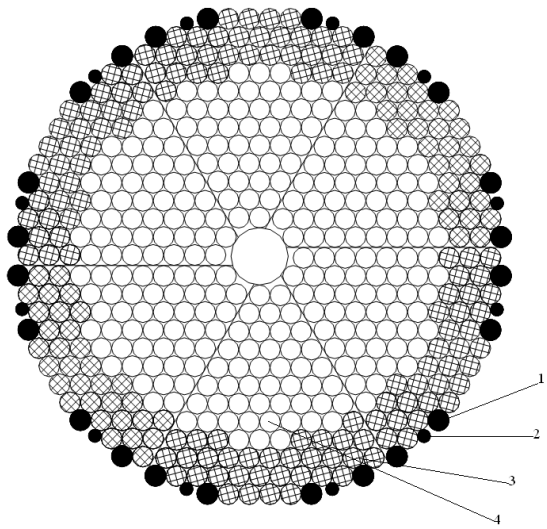

1 – filling material d=2.2 mm; 2 – filling material d=1.6 mm;
3 – fuel elements of peripheral zone; 4 – fuel elements of central zone

Fig. 1. Fuel assembly layout featuring hexagonal pin lattice and filler cylinders. Note that the circular shape denoting the fuel elements is the projected area; the fuel elements are "lozenge" shape, as shown in Fig. 2 (reproduced from Ref. 1).

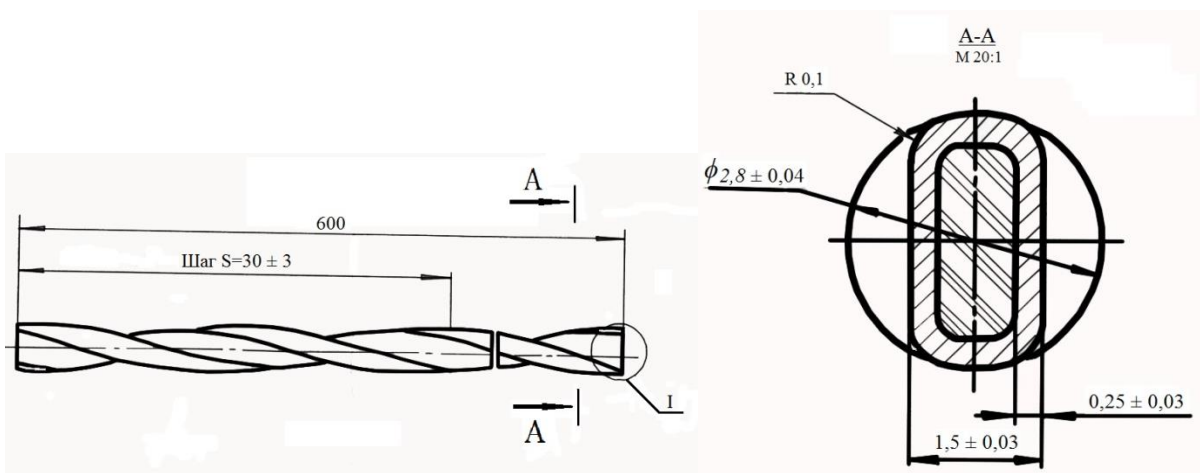

Fig. 2. Specifications for the fuel and cladding (reproduced from Ref. 1).

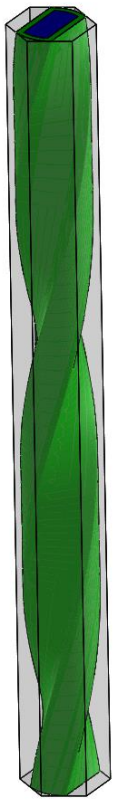

Fig. 3. 3-D view of a single-helical-pitch unit cell.

Table 1. Fuel pin dimensions.

Circumscribed circle diameter	2.8 mm
Blade width	1.5 mm
Helical pitch distance	30 mm
Cross-section of fuel core	1.0 mm x 2.3 mm
Length of fuel core	796 mm for 800 mm assembly; 598 mm for 600 mm assembly
Thickness of fuel casing	0.25 mm around sides

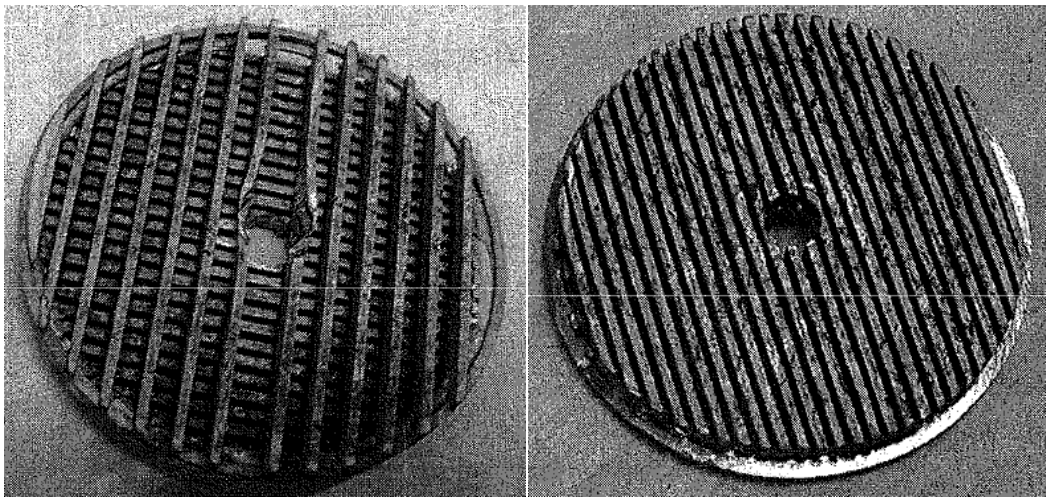

Fig. 4. Geometry of grid supporting the 600 mm pins. Right picture is the pin-facing side (reproduced from Ref. 2).

The coolant for this reactor is water at a rated pressure of 0.8 MPa. The nominal flow rates for the 10MW power are 1.94 kg/s for the 600 mm bundle and 2.1 kg/s for the 800 mm bundle (Ref. 3). The inlet temperature for both cases was 328 K; this is the maximum allowed coolant inlet temperature. The power density, flow rate and pressure combination is such that boiling is not a likely concern during normal operation. For the 10 MW core power, the average flow rate per pin is low enough that the Reynolds number based on the hexagonal pin unit cell is only around 7500. Strong streamline curvature is anticipated due to the twisted pin geometry as well. These conditions can present challenges for standard RANS turbulence models. A further difficulty with modeling the reactor is that, to the authors' knowledge, there are no experimental data with which to compare simulation results. Thus multiple turbulence models should be tested and compared to provide a more confident final result. Uncertainties were measured against the average fluid temperature increase over the domain, which is in the range of 40 K.

Another reason for reducing physics modeling uncertainty is that there are some potentially nontrivial uncertainties in regard to the reactor assembly and pin dimensions. These are due to manufacturing tolerances and other considerations. The exact pin and filler rod positions are not specified, and neither is the individual pin orientation. Given that the pins are not strongly secured in the radial direction, they may also shift or vibrate over time during operation. Given all of these uncertainties, it is important to reduce the physics modeling uncertainty to yield meaningful results for any future sensitivity studies.

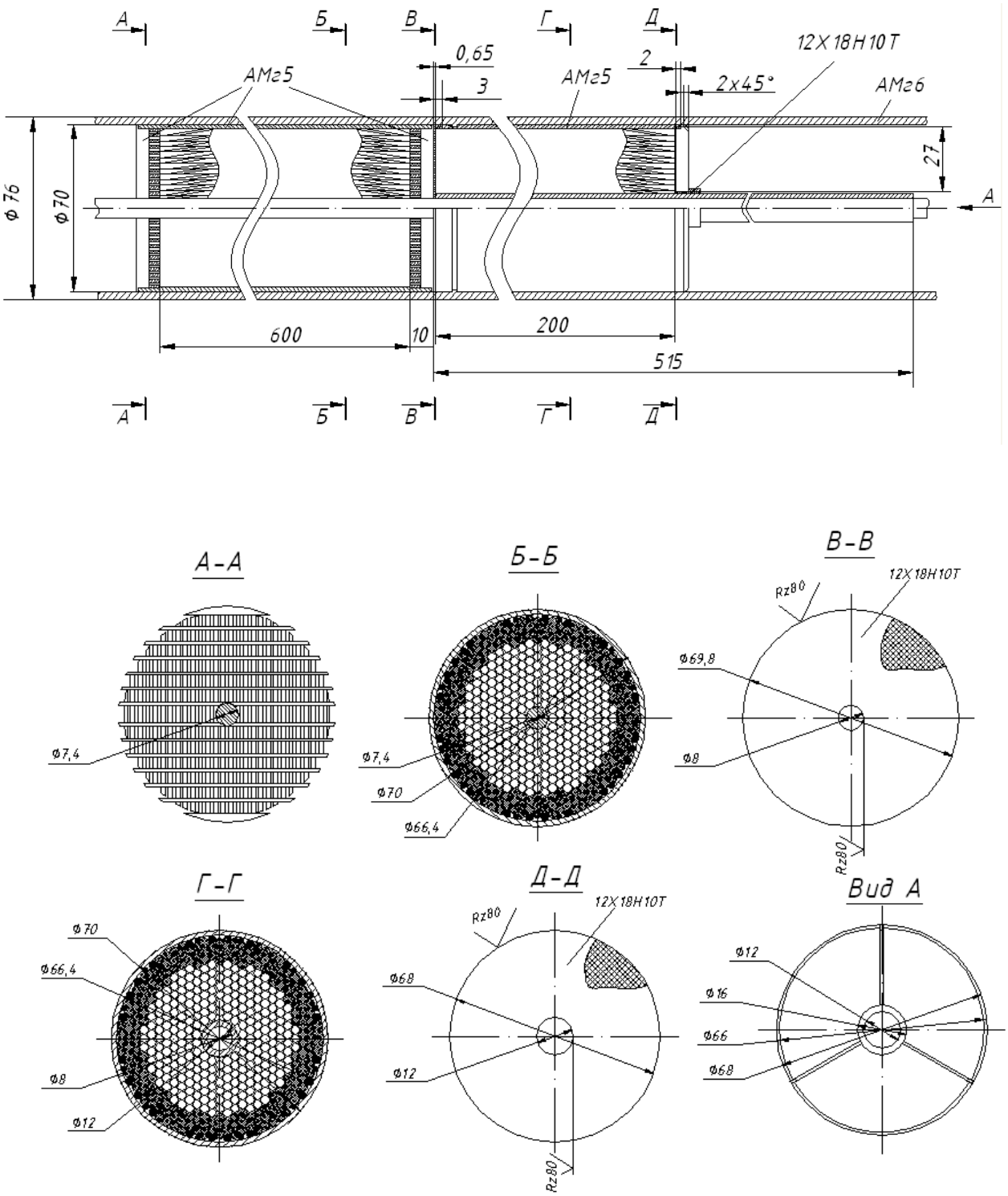

Fig. 5. Diagram of the 800 mm fuel assembly layout, including support grids (A-A) and wire mesh (B-B). Figures not to scale (reproduced from Ref. 2).

III. STEADY-STATE SIMULATIONS

A. Methods

CFD was used to simulate the steady-state operating conditions for both assembly configurations, as well as test transient cases for the single-pin approximation. The majority of simulations were performed using the commercial code STAR-CCM+ v8.04 from CD-Adapco (Ref. 4). The code is capable of solving many multi-physics problems and has undergone extensive testing and validation. It was used here to solve for incompressible fluid flow and heat transfer.

STAR-CCM+ employs the finite volume approach to solve the incompressible Navier-Stokes and energy equations. A suitable grid consisting of primarily polyhedral cells was generated within the code. The grid was based on multiple simulations; the final mesh density was that which showed negligible difference in peak temperature with refinement. The cross-section of a sample grid for a single-pin unit cell is shown in Fig. 6. A layer of prismatic cells was generated orthogonal to the solid walls for the fluid region to improve the accuracy of turbulence and heat transfer modeling. Conformal meshes were created at interfaces of different materials, which was important for the accuracy of conjugate heat transfer modeling between the materials. The mesh count for a full-length 600 mm single twisted pin (fluid and solid regions) was 4.7 million cells, while the 1/6 600 mm sector consisted of 155 million cells. A second-order upwind formulation was used for the convective terms. The SIMPLE algorithm was employed to solve the velocity and pressure equations through a segregated approach.

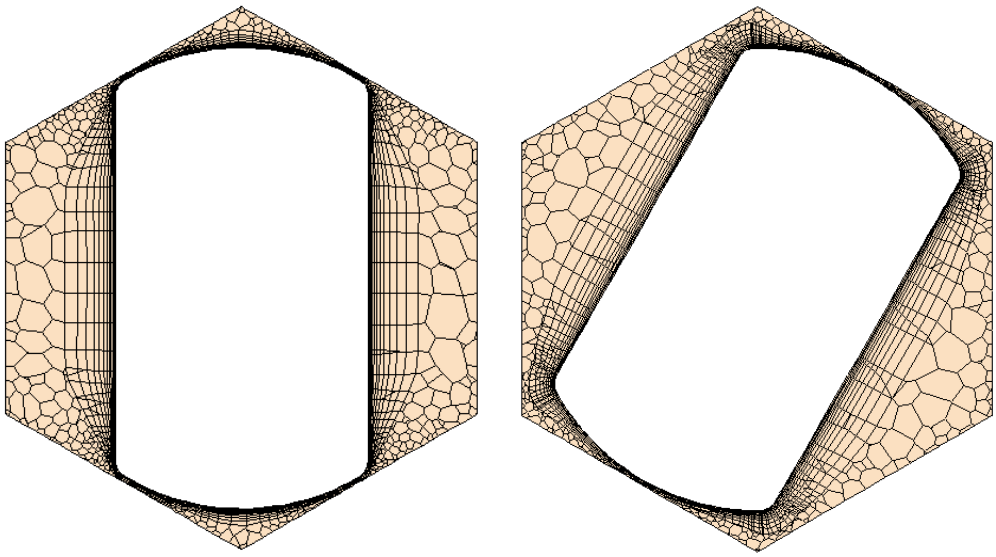

Fig. 6. Example fluid mesh cross-section for the twisted pin unit cell. A large prismatic wall layer is necessary for resolution of the temperature and turbulence there.

In STAR-CCM+, the RANS approach to turbulence modeling was used. Numerous formulations are available to model RANS turbulence, including the well-known k-ε and k-Ω models. Many of the models also have multiple potential wall modeling treatments.

Table 1 lists the turbulence models and wall treatments that were tested. The Low-y+ wall treatment does not make any explicit modeling assumptions in regard to wall modeling, and so the boundary layer must be appropriately refined, with y+ typically below 1. The All-y+ wall treatment, also referred to as the "Two-Layer" treatment, which the STAR-CCM+ manual suggests using whenever available, uses blended wall laws. Although a High-y+ wall treatment (y+ typically around 30 and below 300) was available for some models, it was impractical for this geometry and Reynolds number, particularly since a fine prism mesh is necessary due to the high Prandtl number of water.

Table 2. Turbulence models and wall treatments tested for the single twisted pin.

Model	Wall Treatments
Realizable k-ε Two-Layer	Two-Layer
Standard k-ε Low-Re	Low-y+, All-y+
k-ε V^2F	Low-y+, All-y+
k-Ω SST with curvature correction and Low-Re damping	Low-y+, All-y+

i. 600 mm Assembly

a. Single Pin Simulations

Initial simulations in STAR-CCM+ focused on a full-length, 20-pitch pin unit cell. The cladding wall was contracted slightly so that it would not intersect with the unit cell walls and create mesh singularities. The hexagonal sides of the cell were treated with periodic boundary conditions. An assumption of this approach is that all pins in the assembly have the same orientation. Since no information was available on the pin orientations, this was deemed a valid base geometry before testing the effect of perturbations by simulating a larger assembly section. The inlet was at the top and the outlet was at the bottom of the domain. For single-pin simulations, the fluid domain started and ended flush with the ends of the cladding. The top and bottom faces of the fuel and clad were treated as adiabatic, which is conservative.

Data points from prior neutronics simulations were used to provide a power density shape for the pin. Fig. 7 provides the peak pin power profiles for the 600 mm and 800 mm bundles. A polynomial fit to these data points (12 points for 600 mm pins, 16 points for 800 mm pins) allowed for incorporation of a power density profile with realistic axial variation. No radial variation within a pin was assumed. Integration of this profile over the fuel volume was normalized such that the total power in the pin matched the power in the peak pin. This actually increased the local power density by roughly 4%, so the wall temperature can be assumed to be conservative. The heat source was confined to the fuel region. Constant thermo-physical properties were used initially; fluid properties were evaluated at the expected midpoint temperature. Later, temperature-dependent fluid properties (Ref. 5) were used based on data from the National Institute of Standards and Technology (NIST). The solid properties were constant and were those given in Table 3.

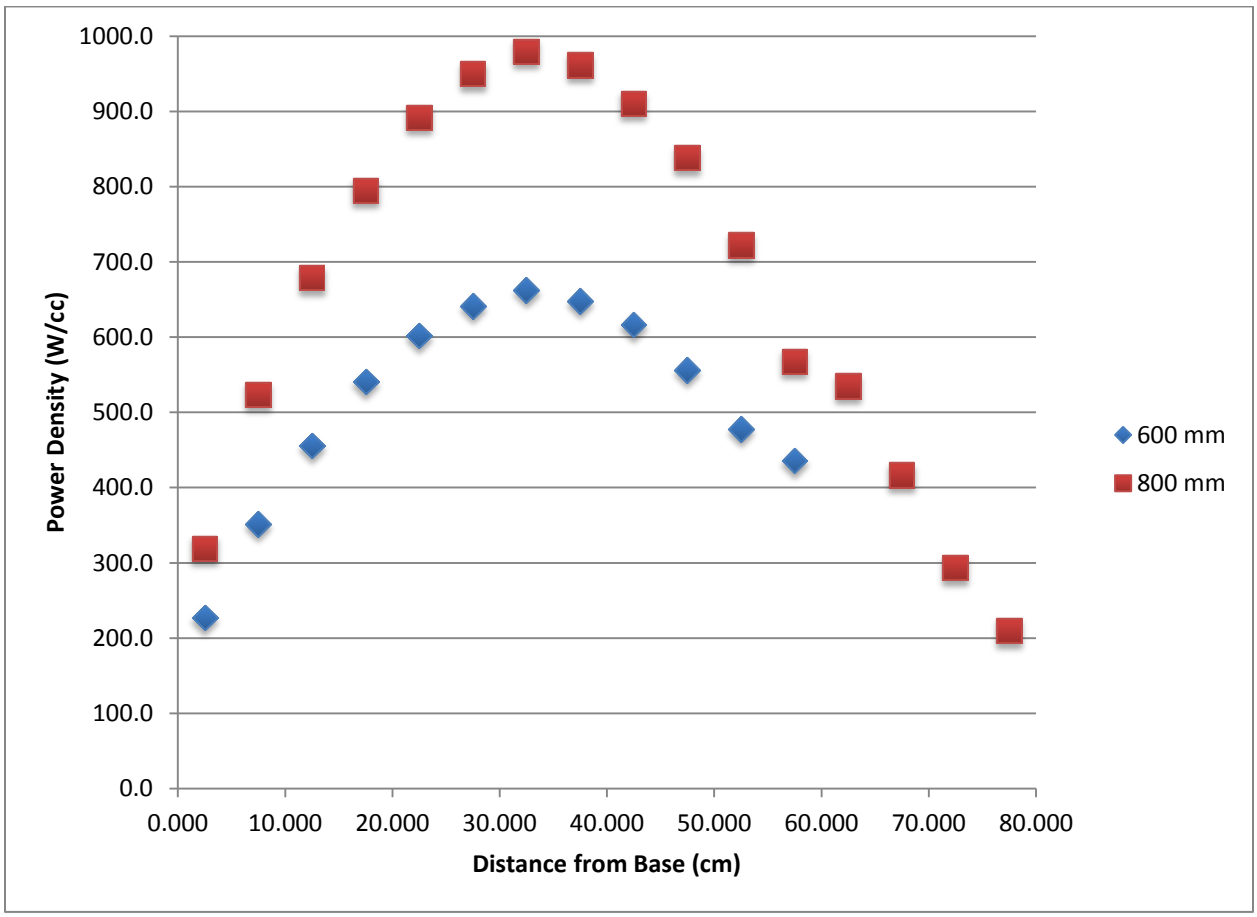

Fig. 7. Radially-averaged axial power density profiles for the peak power pins in both the 600 mm and 800 mm bundles. The support grid is at 60 cm.

Table 3. Material properties for the fuel and cladding.

	U-Zr Fuel	E-110 Casing
Density, g/cc	6.44	7.87
Thermal Conductivity, W/m/K	8.06	18.0
Specific Heat Capacity, J/kg/K	264.07	448.0

As it was found that some RANS models gave different results, and given the lack of experimental data available, higher-fidelity calculations with an LES approach were performed using Nek5000 (Ref. 6). Nek5000 is a massively-parallel, open-source CFD code employing the spectral-element method. LES is an inherently unsteady technique, and so statistical averaging over time of flow parameters was performed to obtain mean and root-mean-square (rms) estimates.

To make the computations more tractable initially, a single helical pitch of one pin with constant thermo-physical properties and periodic boundaries on all fluid sides was simulated. This simulates the "fully-developed" portion of the flow. These runs were hydrodynamics-only and did not include the clad or fuel regions. Simulations of the single pitch were also performed in STAR-CCM+ with RANS and a refined mesh in order to compare the flow fields between RANS and LES (Ref. 7). A further validation run for the wall temperature itself was performed in Nek5000 for a full-length single pin unit cell with temperature-dependent fluid properties. These runs included conduction in the fuel and cladding, and gave a more direct comparison with the STAR-CCM+ results. A hexahedral mesh was generated for Nek5000, shown in Fig. 8. The single-pitch mesh is similar to the full-length mesh except that it is shorter and does not include the fuel or clad.

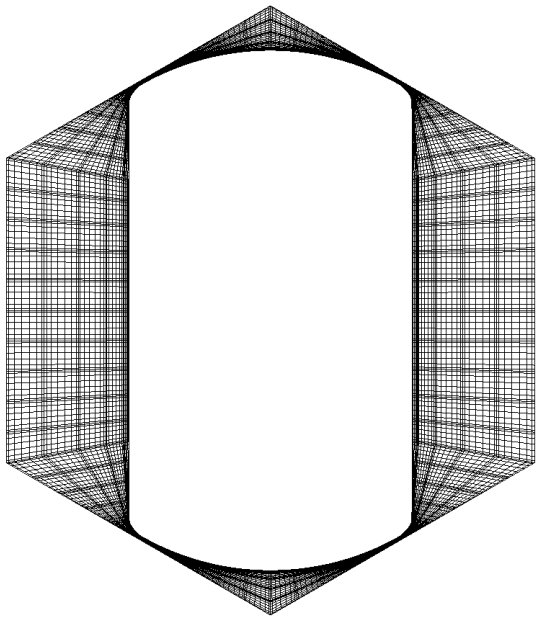

Fig. 8. Nek5000 spectral element fluid mesh cross-section for the single twisted pin.

While Nek5000 is fully capable of performing full-length pin and assembly sector calculations, these would be very computationally expensive. This is compounded by the need to perform sensitivity studies on the geometry, and the potential for runs with higher Reynolds numbers for the high-power operating conditions. The increase in Reynolds number adds significantly more computational overhead for LES than for RANS. Producing hexahedral meshes for the twisted pins is also a time-consuming process. Ideally, the results from Nek5000 and one of the turbulence models in STAR-CCM+ would match well enough that RANS could be applied with confidence to larger sector simulations to reduce the time to results. If no turbulence models agreed with the Nek5000 results, then LES would have to be used to obtain valid results.

b. Assembly Sector Simulations

Methods for the assembly sector simulations were largely similar to those for the single pin. The sector simulations were only run with STAR-CCM+ using the Realizable k-ε Two-Layer model, which was found to be the most appropriate from the single pin simulations. The inner and outer radial boundaries were treated as adiabatic, which is conservative. The sector was 1/6 of the full assembly, and was cut directly through the fuel pins as demonstrated in Fig. 9. The sector was roughly centered around the peak power pin in the bundle. As in Fig. 9, the fluid region inlet was flush with the top of the cladding, while the fluid outlet was extended 90 mm from the cladding base in order to prevent recirculation at the boundary. In order to keep the sector boundaries periodic, the pins on each side must be aligned. This creates a different-shaped flow channel than for the interior pins, and could lead to noticeable boundary effects.

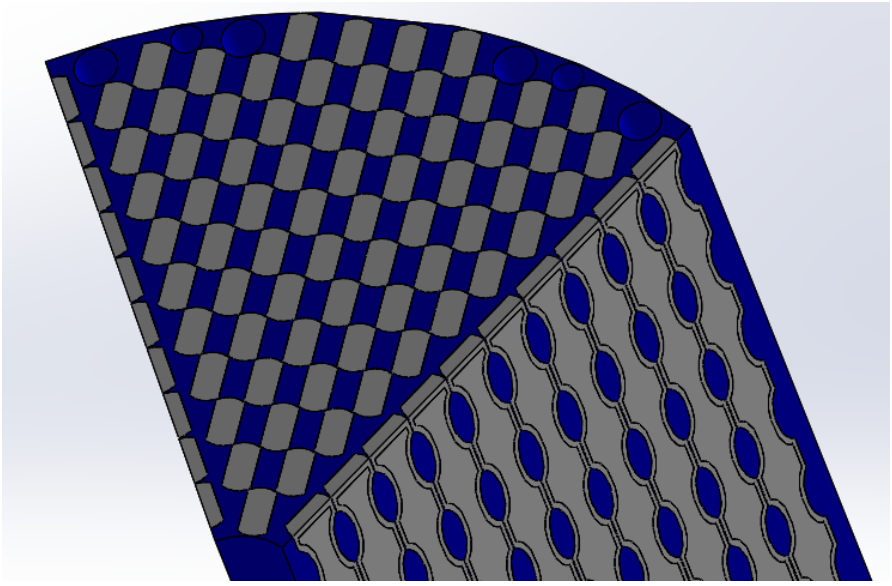

Fig. 9. Geometric model of the 1/6 periodic assembly section. Blue is fluid, gray is fuel/clad.

Since the sector calculations require very large meshes and take a large amount of time to run, efforts were made to reduce the mesh. One key way of doing this was through axial scaling. In STAR-CCM+ there is no way to do this automatically for the unstructured polyhedral mesh generation for the twisted pins. Instead, a smaller axially-scaled model was meshed, and a uniform axial stretching was later applied. Since too great of a stretching for polyhedral cells can reduce solution accuracy, a parametric study of the stretching was first performed on the single pin model. It was shown that a 3x axial scaling could be used without significantly changing the wall surface temperature (~0.1 K difference), so this scaling was used for the bundle meshes.

ii. 800 mm Assembly (HEU Design)

Methods for the 800 mm bundle were largely similar to those for the 600 mm bundle with the exception of the presence of the grid. The main issue with the grid is not its geometric complexity but the fact that it has ¼-symmetry. If the pin region is assumed to have 1/6-periodicity, this means that to perform an appropriate simulation including the grid, one half of the bundle would have to be modeled. Since the pin region is now also one-third larger, this would roughly quadruple the number of mesh cells.

For this reason, the grid was modeled through a porous media approach. The goal was to provide an accurate estimate of the pressure drop while disrupting the flow that had developed prior to the grid, without detailed geometric modeling. To obtain appropriate loss coefficients for the porous media, a ¼-symmetric CFD model of only the explicit grid geometry was built to test its hydrodynamic behavior. Fig. 10 demonstrates the flow-field for a sample grid run.

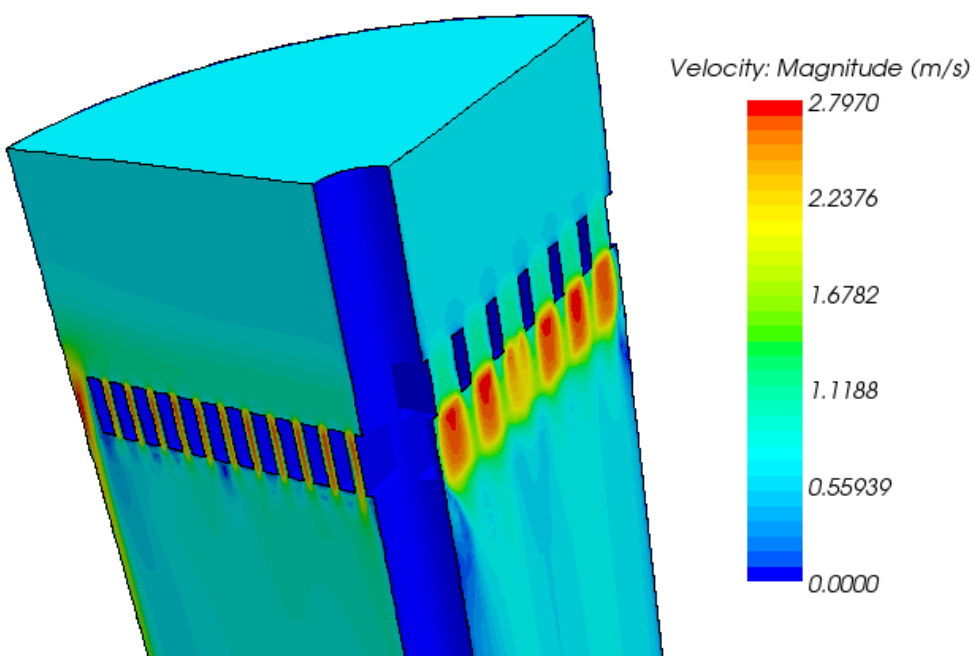

Fig. 10. Example flow through the ¼-symmetric grid model. Refer to Fig. 4 for grid geometry.

The porous media formulation in STAR-CCM+ is given by:

$$\boldsymbol{f}_p = -(\boldsymbol{P}_v \cdot \boldsymbol{v} + \boldsymbol{P}_i |\boldsymbol{v}| \cdot \boldsymbol{v}), \tag{1}$$

where $\mathbf{f}_p$ is the porous momentum source and $\mathbf{P}_v$ and $\mathbf{P}_i$ are the viscous and inertial loss coefficients, respectively. Simulations were performed both with and without the grid for various inlet velocities to obtain pressure loss data points that quantified the effect of the grid. Pressure values were taken 7.5 mm above and 25 mm below the grid. A trendline (see Fig. 18) was drawn through the data points to obtain the loss coefficients. These loss coefficients were implemented only for the streamwise direction, and cross-flow directions had zero resistance in order to smooth out the flow.

The fluid domain was rotated 30 degrees azimuthally with respect to that of the 600 mm assembly in order to keep the peak power pin far from boundaries of the calculational domain. The 200 mm pins on the top of the assembly were also assumed to all have the same orientation. The base of these pins (i.e. the part touching the grid) was assumed to be in alignment with the base of the 600 mm pins. The two pin types both have the same helical pitch. The single-pin runs utilized the power profile of the peak 800 mm pin.

Results for the 1/6 sector straight pin cases demonstrated that the orientation of the pins at the periodic boundaries had a significant influence on the location and magnitude of the peak temperature. To eliminate this issue due to the boundary conditions, full bundle simulations were performed for the straight pins. This was possible only for the straight pins because the uniform cross-section allows for simpler and coarser mesh extrusion in the axial direction, reducing the number of mesh points to a practical level.

B. Single-Pin Results

i. 600 mm

a. Single-Pitch RANS and LES Simulations (Hydrodynamics only)

Comparisons of the turbulence model results were primarily carried out visually, due to the geometric complexity of the flow field. Fig. 11 demonstrates the velocity magnitude profile at the domain midplane for the various models in STAR-CCM+ and Nek5000. The velocity is dominated by the streamwise component. Note that for the single-pin comparisons, the velocities have been normalized by the average streamwise velocity; the turbulent kinetic energy (TKE) has been normalized by the square of the average streamwise velocity. The minimum and maximum values here are those corresponding to the Nek5000 simulations.

The mean flow here is out of the page and in the counter-clockwise direction. The velocity magnitude is generally well-represented by the RANS models with respect to LES. The Realizable k-ε Two-Layer model underestimates the peak velocity with respect to LES, while the V^2F All-y+ model overestimates it. The shapes of the profiles are generally similar between the models. Fig. 12 displays the j-component of the velocity (positive toward the top of the page). This velocity is not as well-modeled as the velocity magnitude, but is still reasonably close to LES. Note that the cross-velocity is perhaps best modeled by the Standard k-ε Low-Re model, which is nearly laminar. This suggests that despite exhibiting some elevated turbulence, this flow may also display some transitional aspects. Fig. 13 displays streamlines for the case. This more clearly demonstrates the general twisting of the flow-field. The bulk flow runs parallel to the

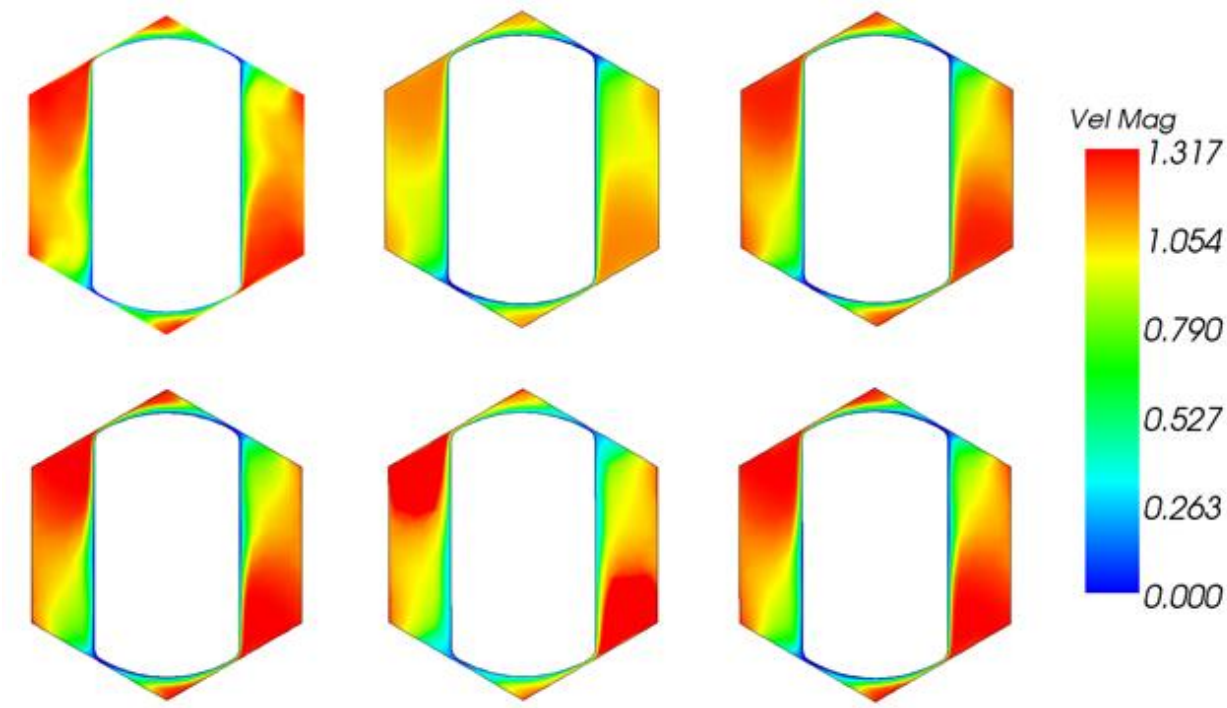

Fig. 11. Velocity magnitude at the midplane for the single twisted pin. Left to right, Top: LES, Realizable k-ε 2-layer, k-Ω SST. Bottom: Standard k-ε Low-Re, V^2F All-y+, V^2F Low-y+.

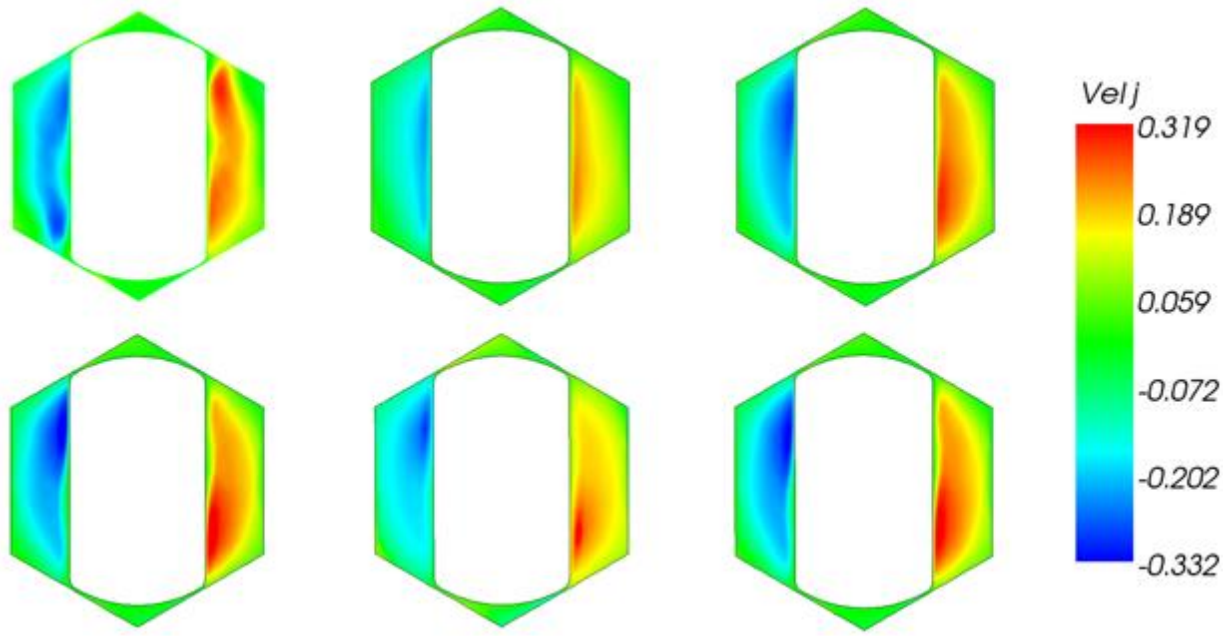

Fig. 12. J-component of velocity (positive toward top of page) at the midplane for the single twisted pin. Left to right, Top: LES, Realizable k-ε 2-layer, k-Ω SST. Bottom: Standard k-ε Low-Re, V^2F All-y+, V^2F Low-y+.

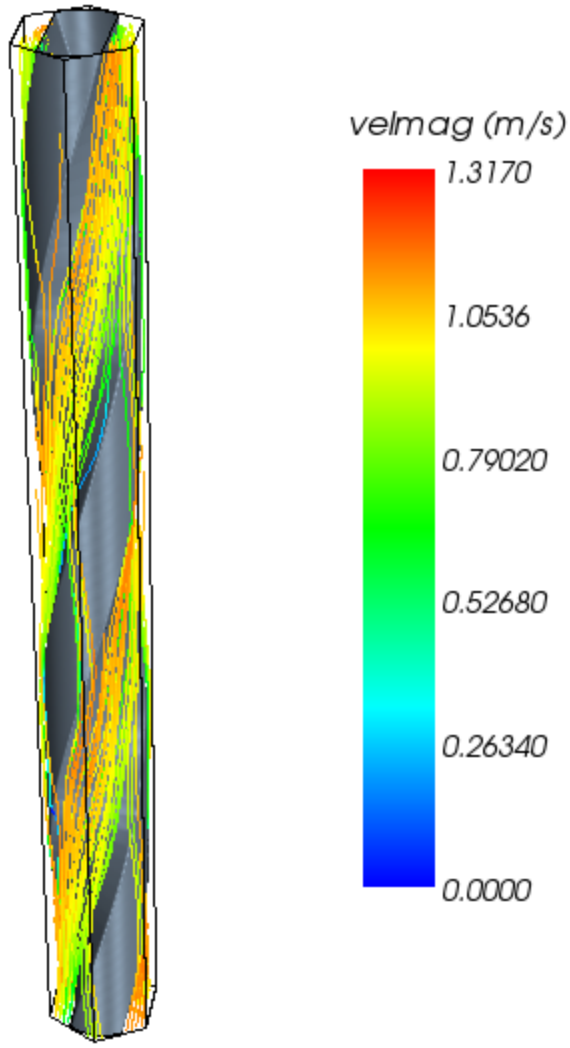

Fig. 13. Velocity streamlines (non-dimensionalized) from the Realizable k-ε Two-layer model in STAR-CCM+ for the single helical pitch case. Note the presence of secondary flows.

long edges of the pin, as expected. The streamlines also show that smaller secondary flow paths exist for which the flow separates from the bulk in the area where the shorter pin edge is near the hexagon corner. This flow then rejoins the bulk further downstream. No large stagnation areas are present.

The TKE estimates show the clearest discrepancies (Fig. 14-Fig. 15) and contribute to the differences in peak temperatures between the models. The bulk TKE from LES is roughly 0.0175. The LES results have low TKE at all four pin corners, while every RANS model has

elevated TKE at two of the corners. The V^2F and Standard k-ε Low-Re models all greatly underestimate the bulk TKE, while the other two models are closer. The Standard k-ε Low-Re model actually has negligible TKE and predicts an essentially laminar flow.

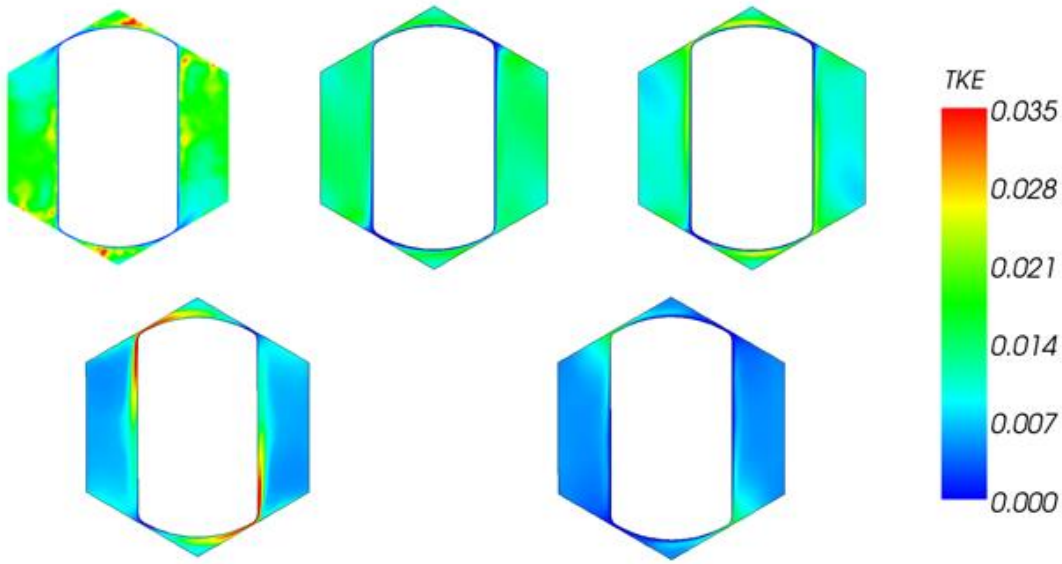

Fig. 14. TKE at the midplane for the single twisted pin. Left to right, Top: LES, Realizable k-ε 2-layer, k-Ω SST. Bottom: V^2F All-y+, V^2F Low-y+. Standard k-ε Low-Re not pictured since it has negligible TKE throughout.

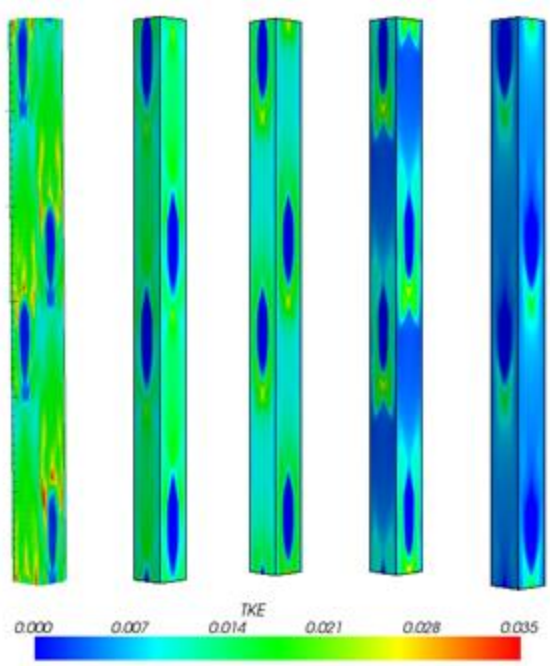

Fig. 15. Vertical TKE profile for the single twisted pin, flow bottom to top. Left to right, Top: LES, Realizable k-ε 2-layer, k-Ω SST. Bottom: V^2F All-y+, V^2F Low-y+. Standard k-ε Low-Re not pictured since it has negligible TKE throughout.

The TKE distribution was shown to be more influential on wall surface temperature than was the cross-velocity distribution, and so it was initially presumed that the models that better matched the LES TKE would have more accurate heat transfer coefficients and hence cladding temperatures. This suggested that either the Realizable k-ε Low-Re model or perhaps the k-Ω SST model would be best for simulating these flow conditions.

b. Full-Length Simulations with Temperature

1. Twisted Pin

Relevant temperature estimates for the full-length single-pin are provided in Table 4 for each of the turbulence models tested. Note that the temperature spread for the cladding surface is roughly 6 K or 15% of the total fluid temperature increase across the domain (40 K). This spread was deemed too large to arbitrarily select a turbulence model, particularly for assessing the impact of geometric perturbations. For this reason, the higher-fidelity LES runs were performed to assist in model selection.

Table 4. Fuel and cladding surface maximum temperature for each of the 600mm single-pin models. Only Realizable k-ε Two-Layer was performed for straight pin. Pin power is 712.4 W.

Model	Cladding Surface Temperature (K)	Fuel Maximum Temperature (K)
Nek5000 LES	371.2	377.6
Standard k-ε Low-Re	375.8	383.1
k-ε V^2F Low-y+	373.7	381.3
k-Ω SST with curvature correction and Low-Re damping	371.8	379.7
Realizable k-ε Two-Layer	371.4	379.3
k-ε V^2F All-y+	369.9	376.4
Straight-Pin Realizable k-ε Two-Layer	372.2	381.2

The peak temperatures generally decrease with higher TKE near the wall (refer to Fig. 14). The temperature profiles between each of the models near the peak are compared in Fig. 16. For every following temperature plot, the horizontal plane is taken at z = 0.075 m, which was in the vicinity of the peak surface temperature. Note that flow here is in the opposite direction, i.e. downward, from that used in the single-pitch runs (orientation did not matter for the hydrodynamics-only runs). The temperature distribution in the fluid follows closely with the velocity distribution; the higher velocity areas generally have lower temperatures and vice-versa. The peak temperature from the LES run was roughly constant over time, indicating that any flow fluctuations had little effect on temperature.

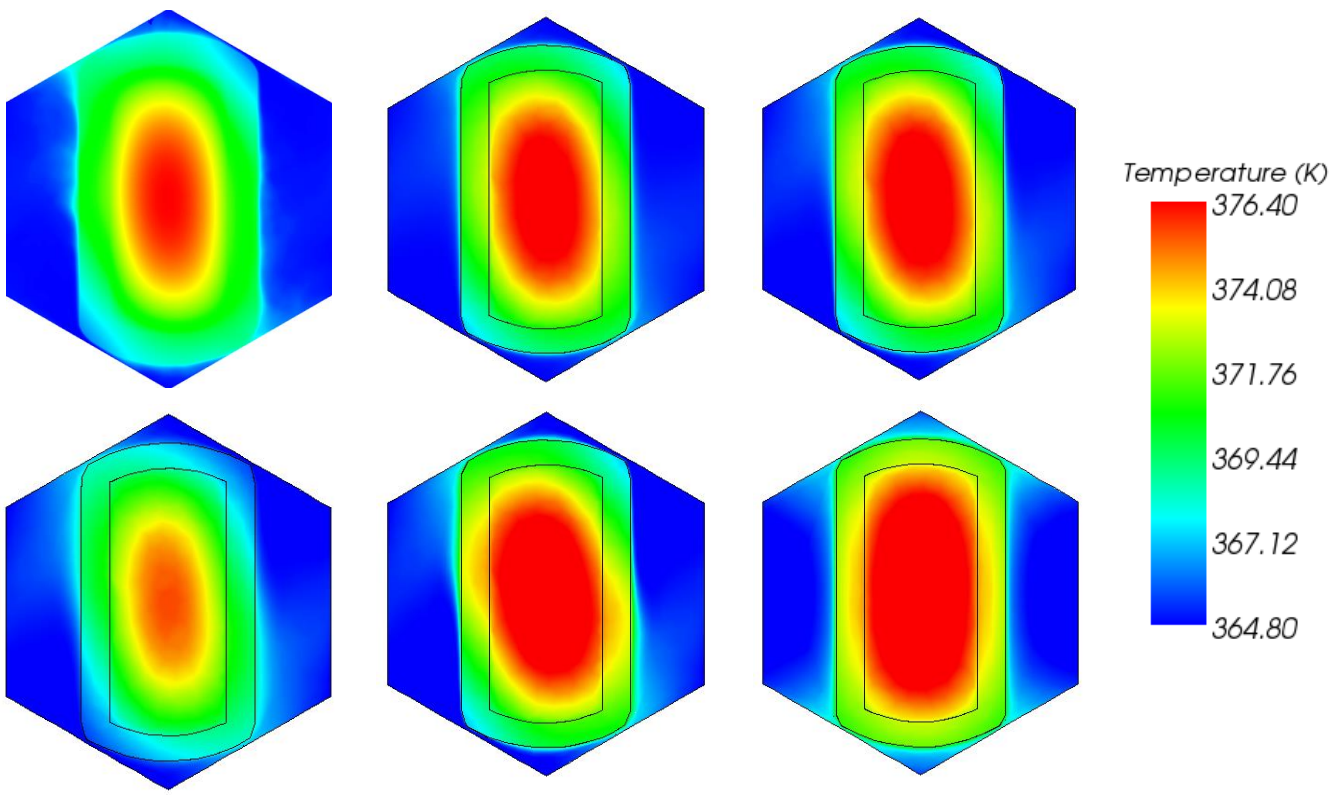

Fig. 16. Temperature distribution at z = 0.075 m for the single twisted pin. Left to right, Top: LES, Realizable k-ε 2-layer, k-Ω SST. Bottom: V^2F All-y+, V^2F Low-y+, Straight-Pin Approximation with k-Ω SST.

The full pin simulation results demonstrate that the Realizable k-ε Two-Layer model is most accurate at predicting surface temperature for these flow conditions, as anticipated from the single-pitch results. This is followed closely by the k-Ω SST model. Results also showed that the flow does indeed exhibit elevated turbulence, and heat transfer is enhanced over pure laminar simulation. For these reasons, the Realizable k-ε Two-Layer model was deemed most

appropriate for these flow conditions and was used for all of the bundle calculations discussed below.

There are some conservative assumptions for the single-pin models, however, notably that using a periodic boundary condition with the peak pin power implies that the surrounding pins also have the same power. This could cause an overestimate of temperature. The peak power pin (for both 600 mm and 800 mm cases) also lies at the outer edge of the assembly, where there is more flow area due to the spacing of the filler rods and such in that region. Thus extra cooling is available for the peak power pin compared to the interior, unit cell approximation. Given the lack of experimental data, the relative influence of these factors can only be properly assessed by performing assembly sector simulations that incorporate the actual pin layout.

2. Straight Pin

Results for the single pin without twisting, utilizing the Realizable k-ε Two-Layer model, are presented in Fig. 17 and Table 4. It is clear, as expected, that the twisting produces additional turbulence and enhances the heat transfer to the coolant. Thus the straight pin has correspondingly higher temperatures. It is worth noting, however, that the straight approximation has a very different flow field from that of the true, twisted pins. This could play a role in determining the location of the peak pin for bundle simulations. Since the cross-sectional area is the same and flow is similar for most of the pin length, non-uniform pin orientation with this approximation may produce local hotspots that would not exist for the twisted pins. Hence the straight pin approximation should certainly be conservative with regard to the maximum temperature magnitude compared to the twisted pins, but may be incorrect with regard to the location of that maximum. The exact location may not be of prime importance, however, for safety evaluations.

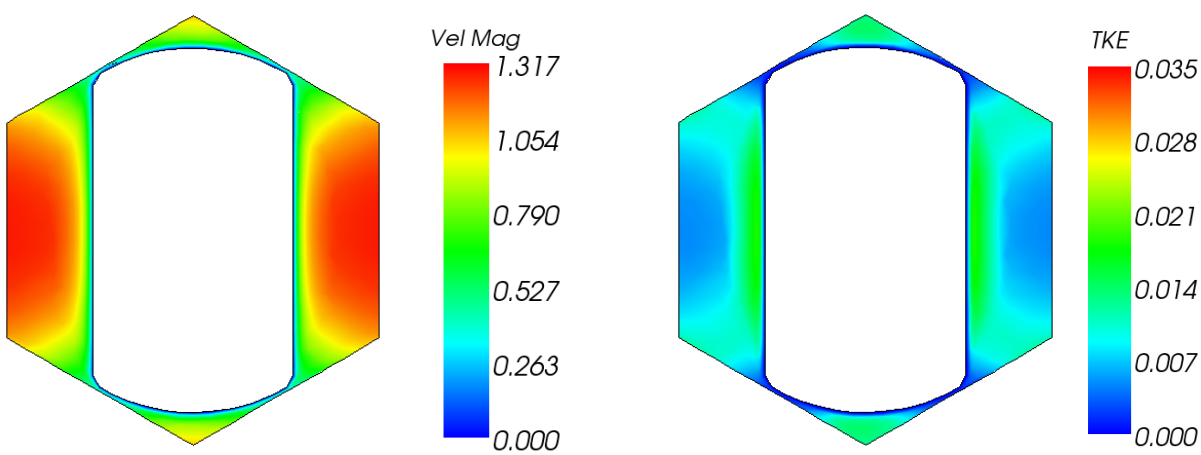

Fig. 17. Velocity magnitude (L) and TKE (R) for the straight-pin approximation. Color scale is the same as for the twisted pin cases above.

ii. 800 mm

The 800 mm pin assemblies feature the highest pin power density, and so are of greater concern for safety. Fig. 18 displays the data from the runs for the grid, and the trendline drawn through them. The porous resistance coefficients were thus determined to be $\mathbf{P}_i$ = 803043 kg/m^4 and $\mathbf{P}_v$ = -42.406 kg/m^3/s. These values were input into the grid region, and the new power profile was used. The exact values were tweaked slightly (but of the same order) to produce a pressure drop closer to that of the stand-alone grid calculation.

Only the twisted single-pin case was run for the 800 mm pin. The peak temperatures for this case are:

- Clad surface maximum temperature = 399.1 K
- Fuel maximum temperature = 410.7 K
- Pin power = 1217 W

As expected from the power density increase, the temperatures are significantly higher than those for the peak 600 mm pin. The peak surface temperature of 399.1 K is still far below the saturation temperature of 443.6 K at the rated pressure of 0.8 MPa. This demonstrates that there is a significant margin to boiling for normal operation, even using the maximum allowed inlet coolant temperature and the normal coolant flow rate. The peak fuel temperature of 410.7K is also hundreds of degrees below the melting point of the U-Zr alloy, supporting the presumption that the fuel temperature is of little safety concern during normal operation. It is important to note that these results are based on one potential core configuration and one possible flow rate (Ref. 3). Thus these results provide relevant data for assessing the general behavior and flow patterns of this type of reactor core and power level, but may not necessarily be representative of the true typical operating conditions.

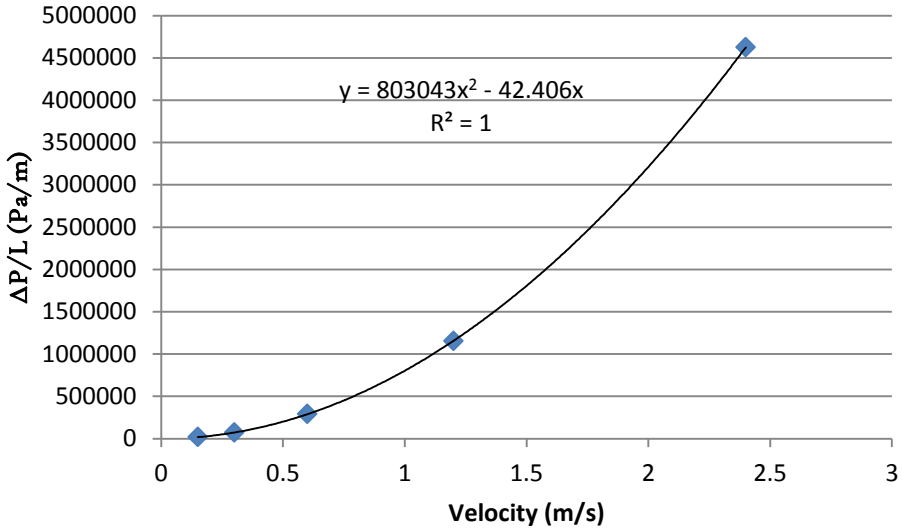

Fig. 18. Data points from support grid CFD results and the trendline drawn to obtain porous resistance coefficients.

C. Assembly Results

i. 600 mm

a. Twisted Pins

The 1/6-periodic sector twisted pin simulations showed that the peak cladding surface temperature for the 600 mm assembly of 370.4 K is less than that from the single pin analysis, suggesting that the single-pin analysis is conservative for the power distribution under consideration. This is largely due to the increased flow area around the peak pin region. Fig. 19 demonstrates that the velocity, and hence cooling, is increased in this region due to the non-uniformity of the spacing at the assembly outer edge. This is also true at the inner wall of the assembly, but the pin power is significantly less there. Thus the peak temperature actually occurs near the middle of the sector (Fig. 20), near the area where the pin enrichment changes. Fig. 21 shows that the cross-velocities for interior pins are indeed similar to those found in the single-pin work, and that the flow for each pin is relatively isolated. This is one reason that the differing orientation of the pins on the periodic boundaries with respect to the interior pins does not create any large temperature discrepancies.

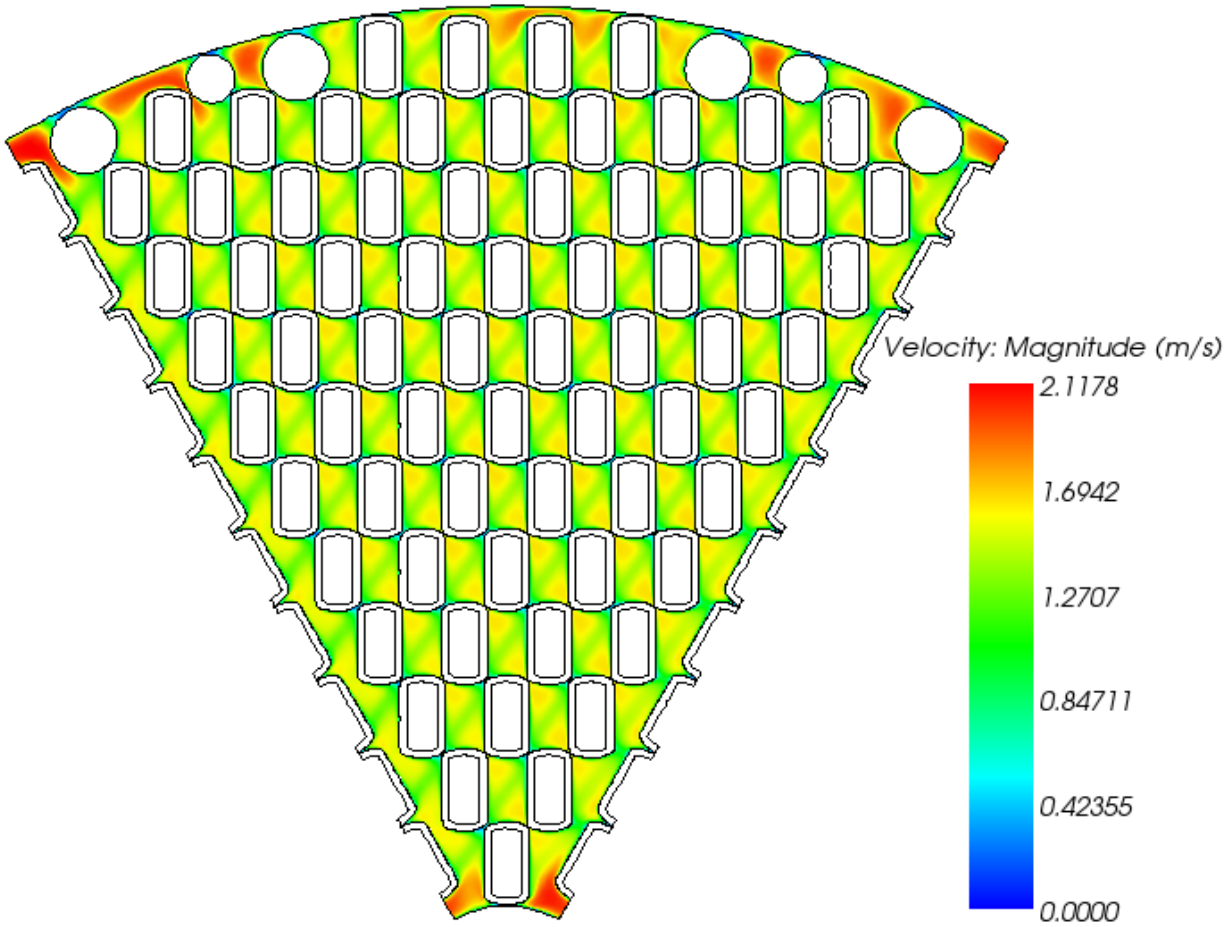

Fig. 19. Velocity magnitude at the midplane for the 1/6 twisted pin case.

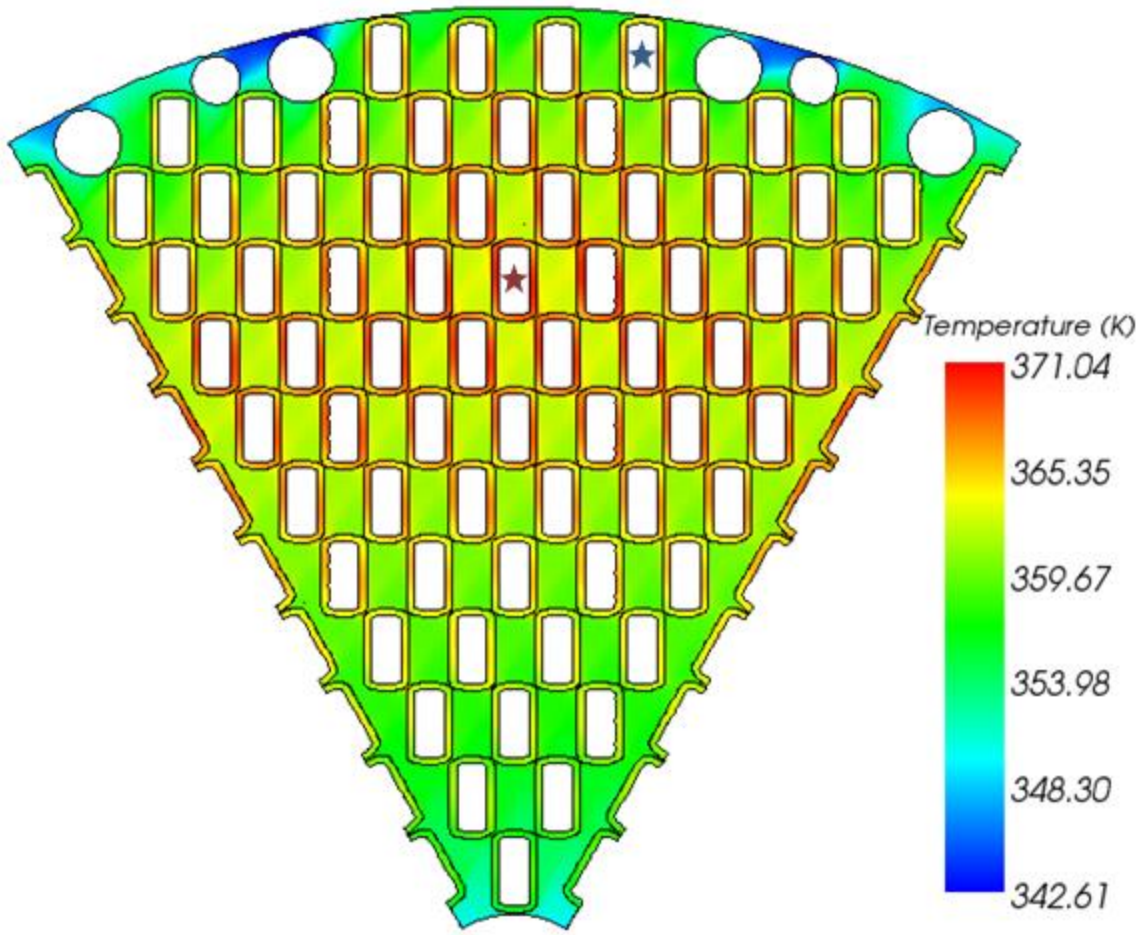

Fig. 20. Temperature at z = 0.075 m for the 1/6 twisted pin case. Blue star is peak power pin, red is peak temperature pin.

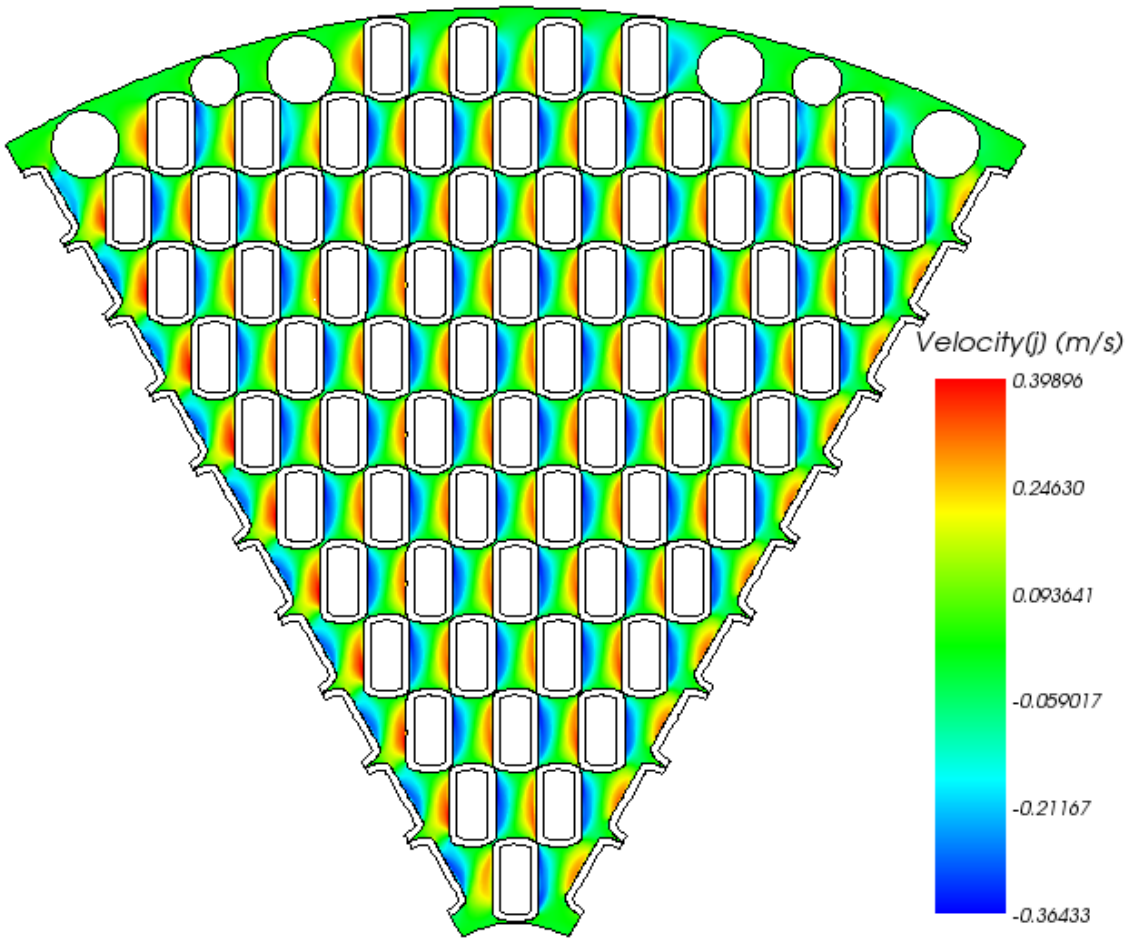

Fig. 21. J-component of velocity (positive toward top of page) at the midplane for the 1/6 twisted pin case.

To further test the effect of pin orientation, a simulation was performed with a randomized orientation for each of the pins in the domain. For the periodic boundary pins, one pin was randomized and the other was rotated 60° from that orientation in order to ensure that the periodic faces matched.

Fig. 22 shows the temperature field for the randomized simulation. The results suggest that the pin orientation does not have significant influence on the peak temperature location or magnitude. The peak pin is in the same location and the magnitude is only different by about 0.1 K from the uniform orientation run, despite having a completely different cross-sectional flow area at a given plane. Thus the uniform orientation, whether true or simply an approximation, is a viable option for simulation and the pin orientation does not have a large effect on the peak temperature behavior.

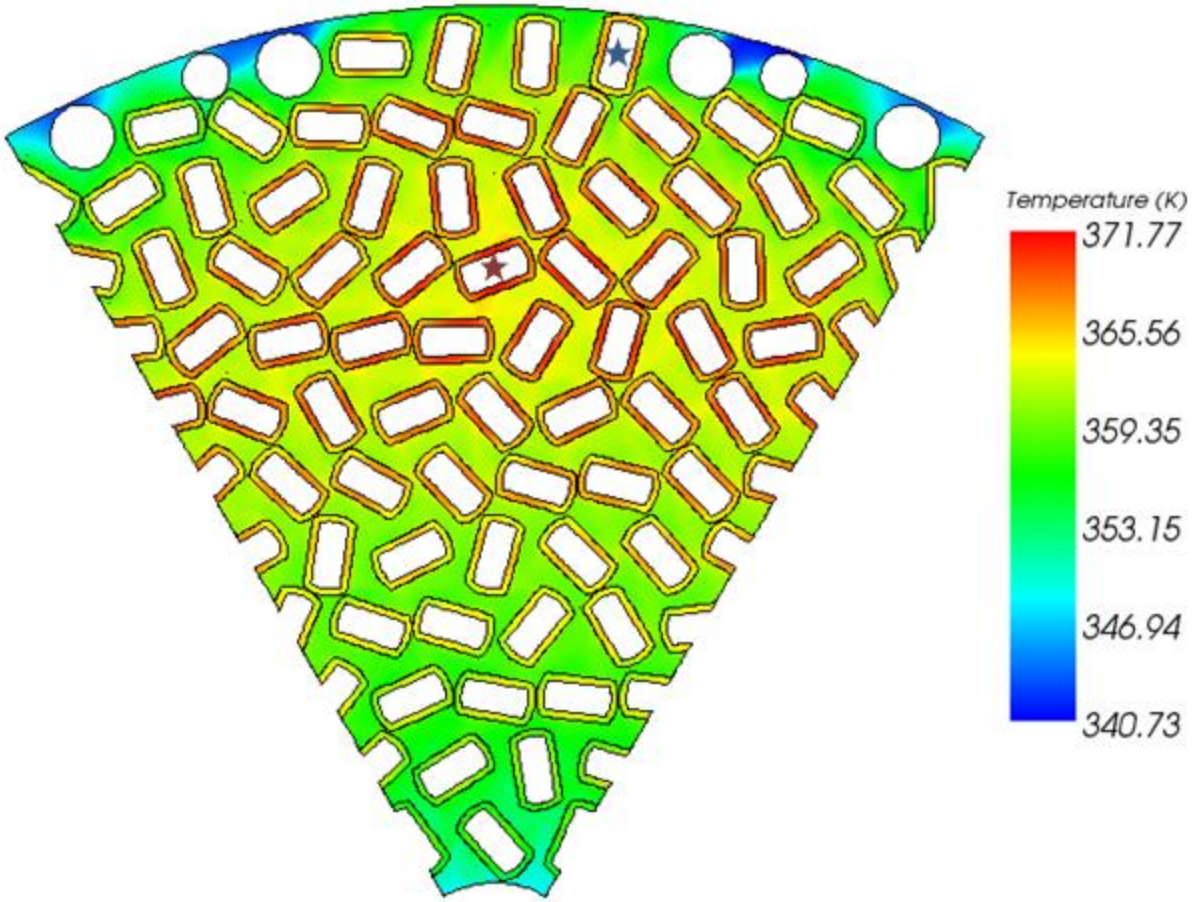

Fig. 22. Temperature distribution at z = 0.075m for the randomized orientation 1/6 twisted pin case. Blue star is peak power pin, red is peak temperature pin.

b. Straight Pins

Initial 1/6 sector simulations for the straight pin approximation were performed with pins in the same layout as those for the twisted case, but it became apparent that the boundaries and pin orientation played a more substantial role in determining the peak temperature than for the twisted pins. In Fig. 23, the peak cladding temperature occurs at a periodic-boundary pin due to the pin orientation there. The short ends of the two boundary pins are in very close proximity for their entire length, and cooling is greatly reduced in that area. Thus despite having a significantly lower power density and being relatively far from the peak power pin, one of these pins has the peak temperature.

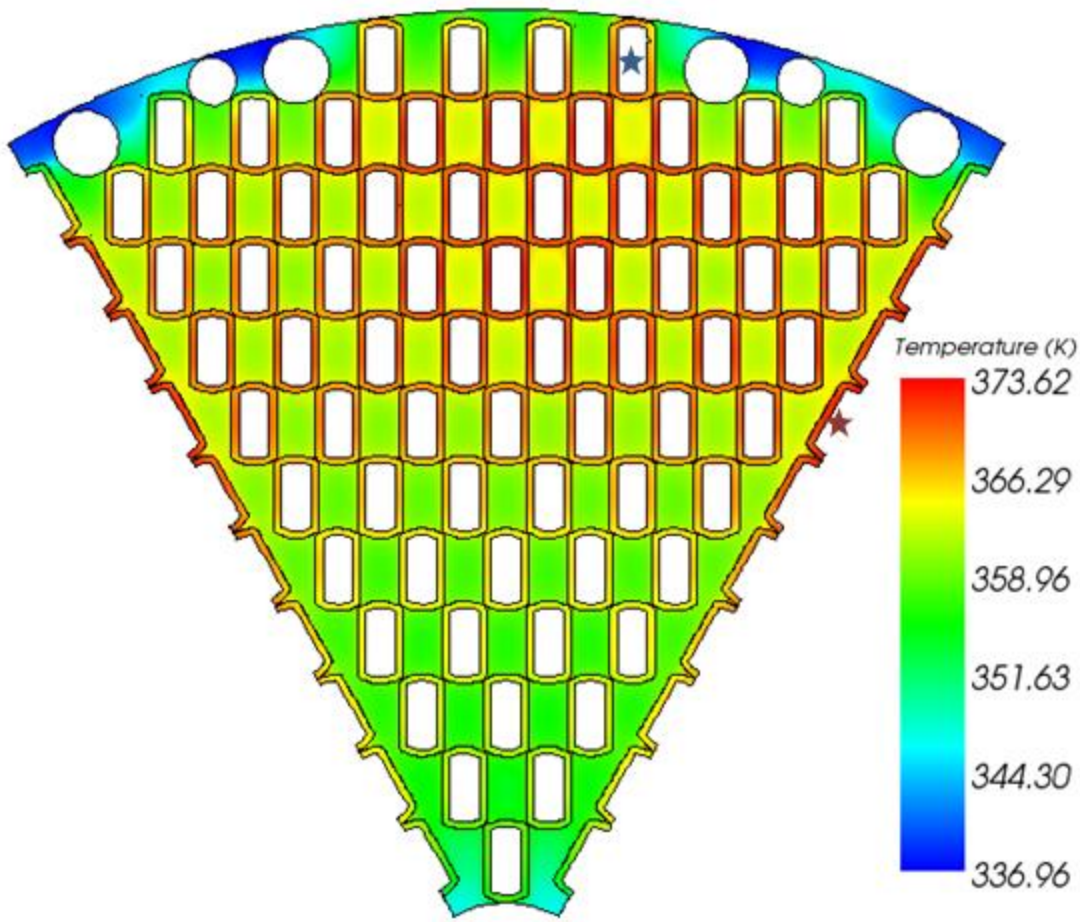

Fig. 23. Temperature distribution for the 1st orientation of the 1/6 straight pin case. Blue star is peak power pin, red is peak temperature pin.

Another simulation was run with a different orientation for the periodic-boundary pins. Fig. 24 demonstrates that the peak temperature magnitude is similar but the pin location has changed, and is still near a periodic boundary. To eliminate the effect of the periodic boundaries, full bundle simulations were then performed. Pin orientation was uniform throughout the domain for these simulations. While the periodic boundary influence was removed, it was found that the flow area difference due to the filler rod placement and pin orientation still had significant influence. Fig. 25-Fig. 26 display how the smaller flow area for one of these pins contributed to it being the peak temperature pin. These consistent boundary issues suggest that the straight pin approximation should be used with care, particularly in regards to pin orientation, in order to obtain meaningful results.

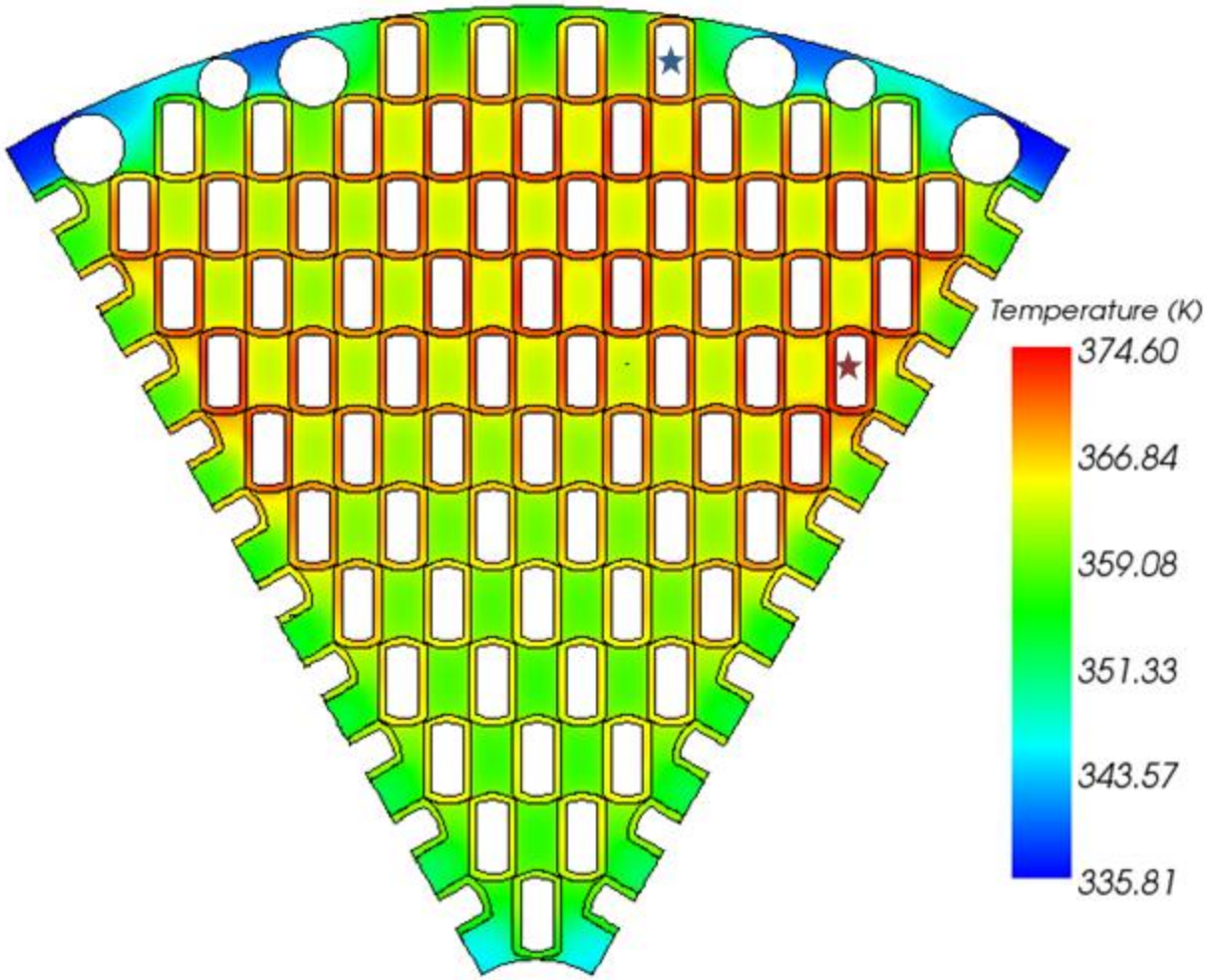

Fig. 24. Temperature distribution for the 2nd orientation of the 1/6 twisted pin case. Blue star is peak power pin, red is peak temperature pin.

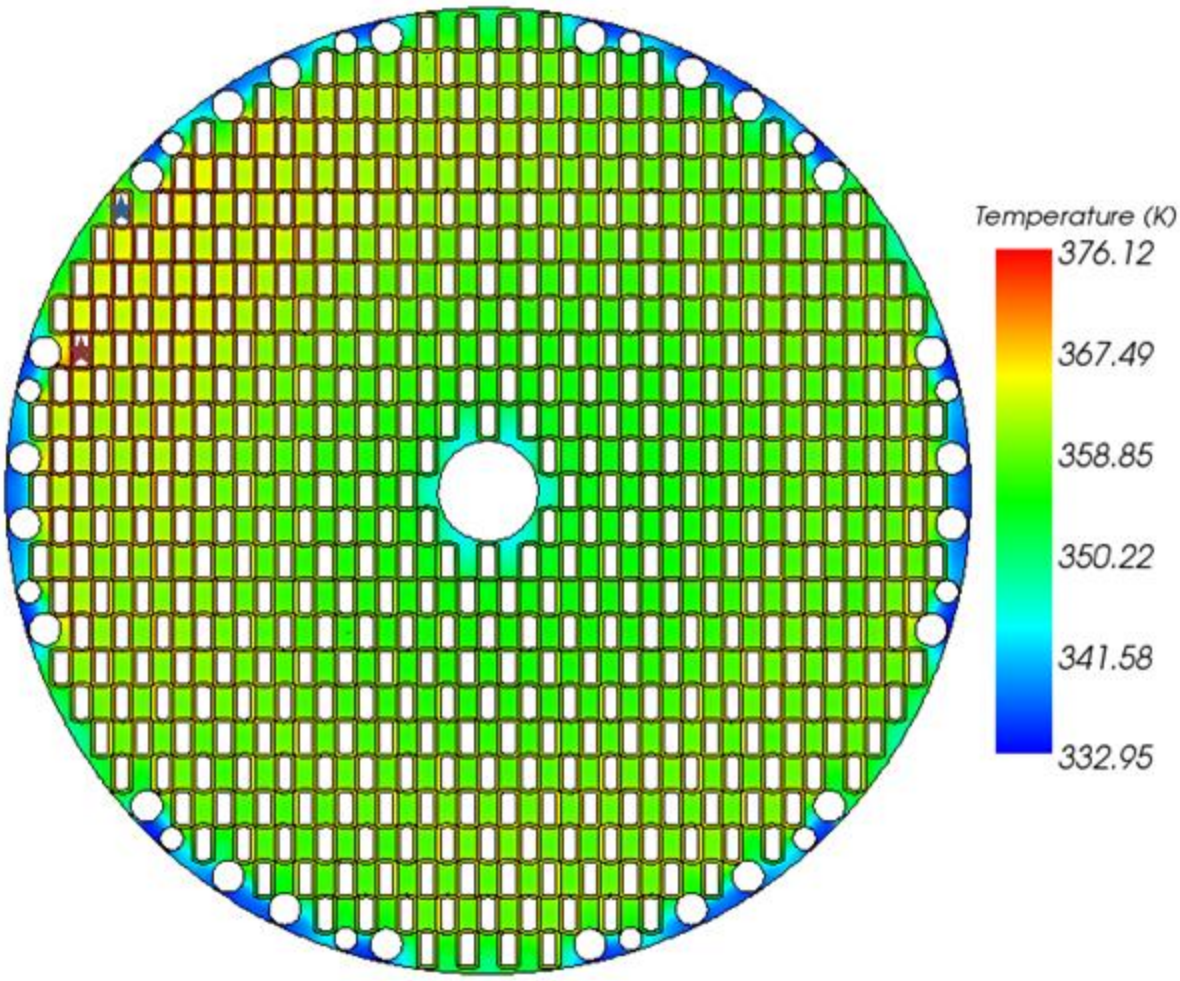

Fig. 25. Temperature distribution for the full-bundle straight pin case, eliminating periodicity boundary condition concerns. Blue star is peak power pin, red is peak temperature pin.

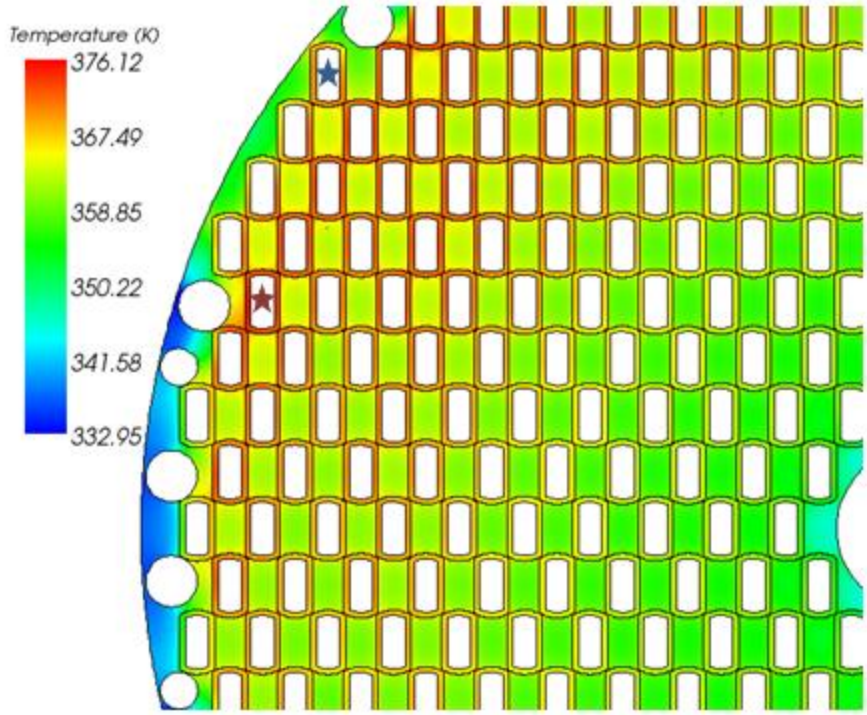

Fig. 26. Zoomed-in view of the full-bundle straight pin case. Blue star is peak power pin, red is peak temperature pin.

Table 5 provides a summary of the peak temperatures for each of the twisted and straight pin 600 mm results. Again, the straight pin runs are more conservative than the twisted pin runs, as anticipated. Additionally, the single twisted pin is more conservative than the twisted pin bundle, which could potentially cut down simulation and meshing time if this is found to be true for further test cases. It should be stressed, however, that the single straight pin is not necessarily conservative with regard to the straight pin bundle. The boundary effects and orientation are much more important than for the twisted pin, meaning that the periodic unit cell for the straight pin is not an arbitrarily good representation of the peak temperature regions in the real bundle.

Table 5. Summary of clad surface temperatures for each of the 600 mm geometries tested.

	Single Pin Twisted	1/6 Twisted Uniform	1/6 Twisted Random	Single Pin Straight	1/6 Straight Orientation 1	1/6 Straight Orientation 2	Full Bundle Straight
Max clad surface temperature (K)	371.4	370.4	370.5	372.6	373.2	373.3	374.7

The fundamental differences between the straight and twisted pins are important to note. The twisted pins are in close contact with other pins or boundaries at only roughly 40 points over their length (two per pitch, 20 total pitches). If a straight pin is in close contact with another boundary, however, it is in close contact for its entire length, creating a larger region of reduced flow area. For the full bundle, it is possible the pins could be oriented in such a way that no pin was in very close contact with another pin or boundary. This would be an arbitrary fix, however, and still may not lead to identification of the true peak temperature location.

It should be noted that although the straight pin approximation is not reliable for predicting the peak temperature location, this may not be of strong concern. The approximation is consistently conservative. The twisted pin results also demonstrate that a number of pins have maximum temperatures close to that of the peak pin, so the exact maximum location may not be crucial. Hence the straight pin approximation could still prove useful for some scenarios.

ii. 800 mm

The 800 mm pin bundle results corroborated many of the findings from the 600 mm runs. For the 800 mm pin bundle, only the twisted pin case was investigated. The peak temperatures were:

- Clad surface maximum temperature = 391.6 K
- Fuel maximum temperature = 403.0 K

Velocity distributions were generally similar to those in the 600 mm case due to having a similar geometry. The peak temperature of 391.6 K was more significantly below that from the single pin simulations than for the 600 mm case. This is due to the peak power pin in the 800 mm bundle being in a different location than that of the 600 mm bundle. This location actually has an even greater cooling area relative to the unit cell, and fewer fuel pins surrounding it. These extra factors are not accounted for in the single pin model. The temperature field is provided in Fig. 27. The peak temperature location is actually very close to that in the 600 mm case. This is again roughly the area where enrichments change, and is an interior pin. This suggests that the single-pin model may again be a useful tool in reducing the simulation/meshing time while still obtaining relevant and slightly conservative results.

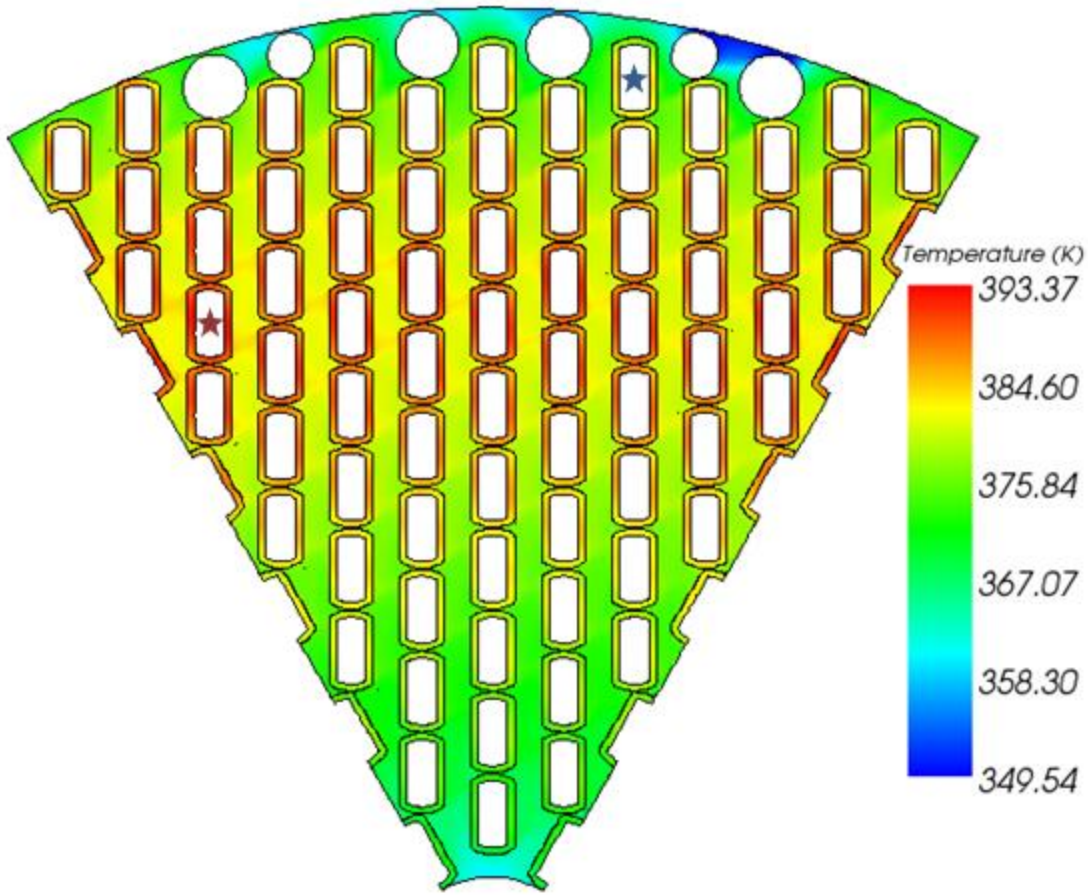

Fig. 27. Temperature distribution at z = 0.075 m for the 800 mm twisted pin case. Blue star is peak power pin, red is peak temperature pin.

IV. TRANSIENT SIMULATIONS

A. Methods

Many of the significant safety concerns for a reactor involve transient effects. CFD is not practical for many of these dynamic simulations, particularly for long transients and large, complex reactor systems; the computational expense is too great. CFD can also struggle to deal with boiling and other multiphase phenomena frequently present in reactor accidents. For this reason, system codes such as RELAP5-3D (Ref. 8) are typically used to simulate the dynamic system response with reasonable calculation time and accuracy. CFD can be used, however, to evaluate the RELAP results and confirm that the selected convection heat transfer coefficient and other parameters in the RELAP input are reasonable.

Two different test transient scenarios were investigated here. Both limit the domain to a single-pin unit cell for practicality. The first scenario (the “slow” or “ramp” transient) compares the 800mm twisted-pin CFD model in STAR-CCM+ to a RELAP model using a cylindrical pin. The cladding outer radius (1.24 mm) in the RELAP model was chosen so that the cladding outer surface area was the same as in the twisted-pin CFD model in order to preserve the heat flux. The cladding inner radius (0.96 mm) and fuel inner radius (0.44 mm) in the RELAP model were chosen so that the cladding and fuel volumes were the same as in the twisted-pin CFD model in order to preserve the thermal inertia during a transient. The RELAP model is shown in Fig. 28. The power increased from 50% to 100% of nominal (1217 W) in a linear ramp over 10s; this is the power for the peak single pin at 10 MW core power. There is no mechanistic basis to support power doubling over 10 s; the conditions were chosen merely to investigate transient behavior in the codes. Inlet temperature was 293 K so as to avoid any boiling.

The second scenario (the “fast” or “step” transient) compares the dynamic responses of the different CFD models constructed by ANL and IAE, as well as a cylindrical-pin RELAP model. The IAE model was of a twisted single pin, modeled with ANSYS CFD. The ANL CFD models consisted of the standard twisted-pin model as well as a cylindrical pin model constructed much like that for the scenario described previously. This cylindrical model, which did not include any modeling of the grid and so had one continuous 800mm pin, was constructed to have a more direct comparison with the RELAP model. The hexagonal fluid cell dimensions in the cylindrical model were changed such that the flow area, and hence average velocity, was the same as for the twisted pin model. For this scenario, IAE specified that the core power promptly increased by 0.5 MW from 1.724 MW to 2.224 MW. No mechanistic basis for this power increase was stated; it is merely a set of conditions to test transient models. For the single pin, it was assumed that the power increased by the same ratio, corresponding to an increase from 122.8 W to 158.4 W for the average (not peak) power pin. The power profile shape for this transient was taken directly from Fig. 17 in Ref. 9 to more directly compare with IAE results. The inlet temperature was specified as 309.25 K.

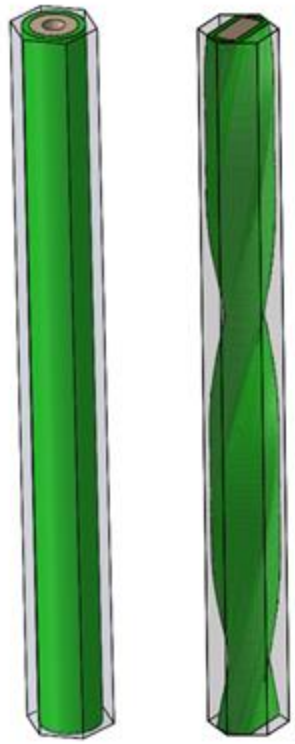

Fig. 28. Geometric model for hollow cylindrical pin in RELAP, displayed with twisted-pin model for comparison.

For both scenarios, the single-pin flow rate of 4.3 g/s (corresponding to 62.37 kg/s core total flow rate) and the inlet temperature were kept constant throughout the transient. Polynomial expressions for water properties based on temperature were used in both RELAP and STAR-CCM+. The water properties were confirmed to have only small deviation between the codes. Constant properties were used for the solid domains in the "slow" transient, while variable solid properties were used in the "fast" transient. Density was constant in all simulations. For the second scenario, the fuel and cladding were both treated as having the material properties of the cladding (to be consistent with the modeling in Ref. 9). Initial conditions were obtained by running a steady-state (SS) case for the initial power level. The transients were then run until a new SS was reached. The power profile shape in each case was kept the same, and magnitude increased by imposing an axially-uniform factor on the original profile. The power was distributed within the fuel only for all models.

B. Results

i. "Ramp" Transient

Fig. 29 displays the results from the CFD and RELAP ("Case 49") models for the transient ramp. The new SS is reached after about 11.5 s, or 1.5 s after the end of the ramp (ramp starts at t = 0 s). Temperature increase is largely linear as expected, with nonlinear transient effects at the start and end of the ramp due to thermal inertia. Temporal behavior is similar between the two runs. Maximum cladding surface temperature, the value of most concern for safety in this reactor, is slightly higher (~0.5 K) for RELAP but acceptably close.

Fig. 30-Fig. 31 also demonstrate that the temperature behavior is generally similar for the two models at multiple axial locations over time. In the area just downstream of the grid, which was modeled in CFD but not in RELAP, there are differences between the temperatures. This is due to the grid changing the flow pattern in this area. The flow develops soon after though, and values match very well in the peak temperature area of the pin.

Additionally, a comparison of step vs. polynomial power profile interpolation was performed for CFD (Fig. 29). RELAP can only use a step input, meaning that the power density is constant over the axial node length, which is 50 mm in the current case, which matches the neutronics data noding. But a polynomial interpolation is frequently more appropriate for CFD given the fineness of the mesh and relative coarseness of the neutronics data points. As shown, the step profile for STAR-CCM+ does indeed yield closer peak temperatures to those of RELAP, but these are within acceptable range of the polynomial temperatures as well. The step profile is also slightly conservative (i.e. results in a higher peak cladding surface temperature) as compared to the polynomial profile. This all provides evidence that the RELAP model using the standard Dittus-Boelter correlation for the convective heat transfer coefficient yields good results as compared to the CFD model for this type of transient.

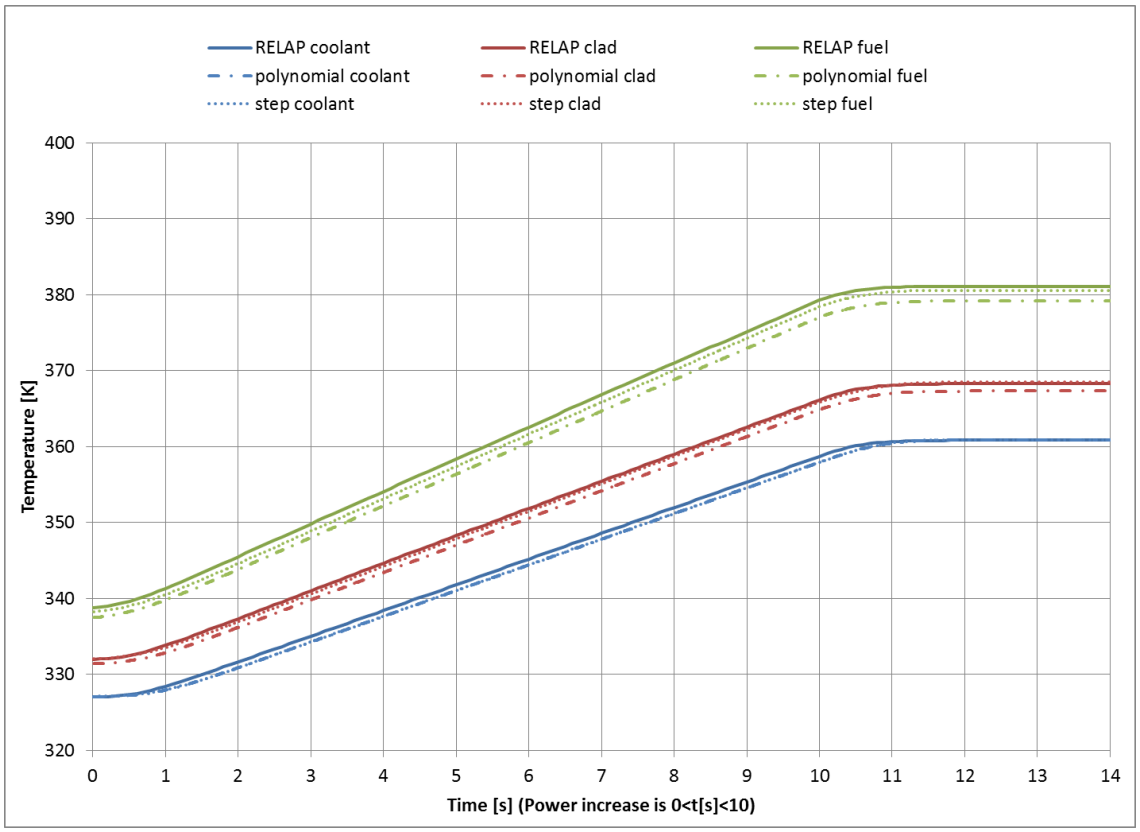

Fig. 29. Peak temperature results for linear ramp. Solid lines are RELAP, dotted lines are CFD with step power interpolation, dot-dashed lines are CFD with polynomial power interpolation.

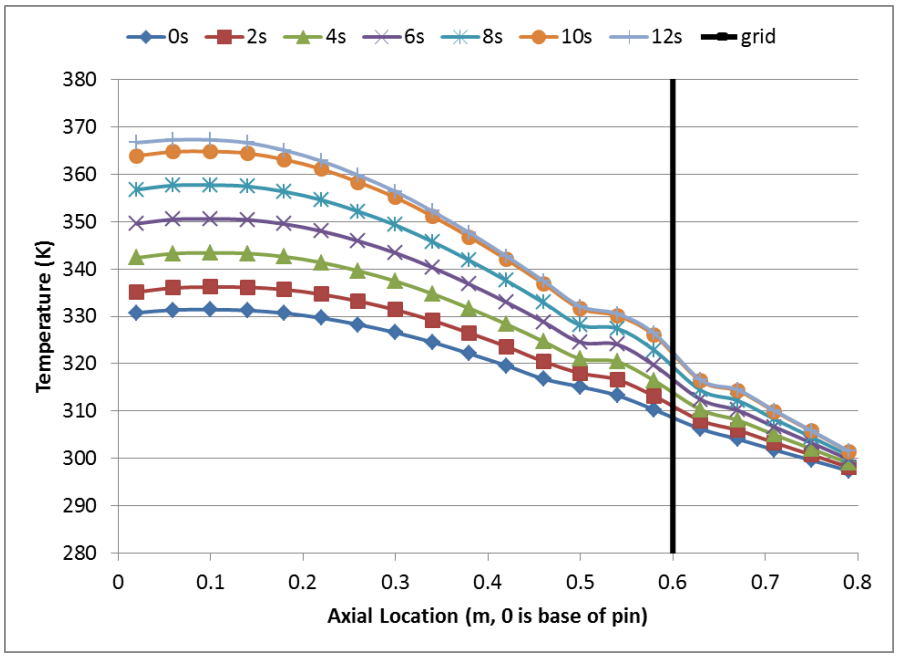

Fig. 30. Cladding surface temperature axial profile over time for CFD.

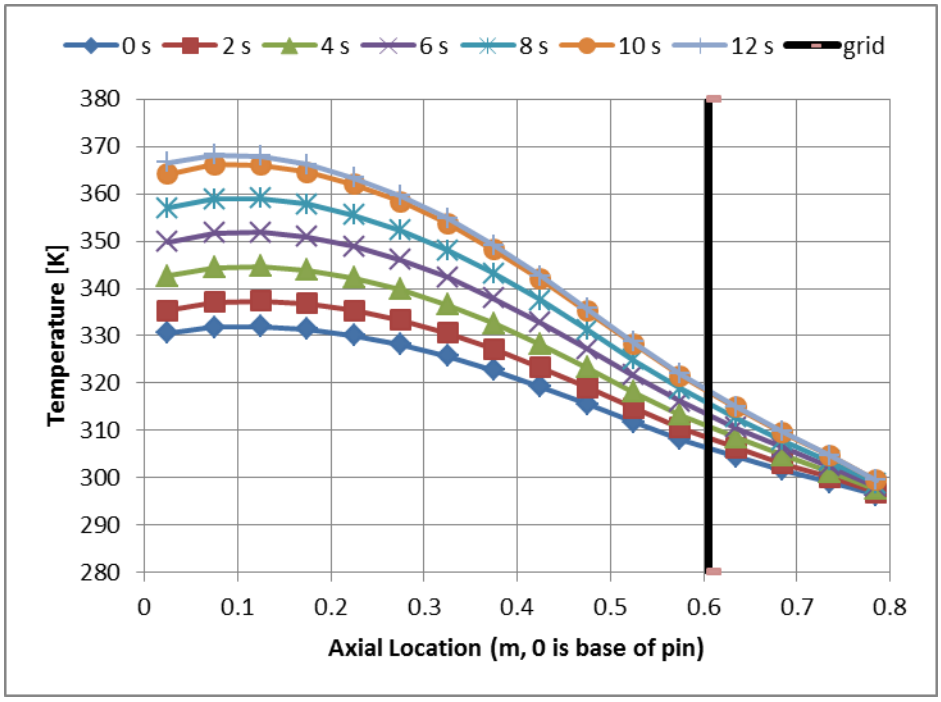

Fig. 31. Cladding surface temperature axial profile over time for RELAP.

ii. "Step" Transient

The IAE results gave volume averages of the cladding temperature over a 1 mm length at four different heights (cladding surface temperature could not be easily extracted). The history of the coolant outlet temperature was also recorded. Table 6 summarizes some key results for each of the different models, which are also presented graphically in Fig. 32-Fig. 33. Steady-state for these results was defined to occur when a temperature was within 0.05K of its final value. Temperatures were averaged over 1 mm for the ANL CFD case, while for RELAP the representative "average" was limited to the node size (10 mm for the fine "Case 52", 50 mm for the coarse "Case 50"). The RELAP cladding results are for surface values.

All of the models have roughly identical initial and final coolant outlet temperatures, indicating that the total power increase was matched. The ANL models all have general agreement with the temperature magnitudes of the IAE model, with the twisted pin being closest as expected. The RELAP model and the ANL CFD cylindrical feature somewhat higher temperatures. The node size was intentionally reduced in the 10 mm-node case in order to make agreement between the RELAP and CFD models as good as possible, but this is much finer than would normally be employed. Smaller nodes increase the accuracy of the numerical method, while also being closer in spacing to the 1 mm used in the CFD cases. While it was shown that decreasing the axial node

size in RELAP does reduce temperatures for this case (Fig. 34), it does not lower them enough to warrant the increase in computational time. The twisted pin model was assumed to be the "gold standard", since it featured the most accurate geometric representation and physics.

The ANL CFD twisted and RELAP models agree better when comparing the peak temperatures instead of the averages at a few levels, as shown in Fig. 35. These peak temperatures are most important for safety. The time to reach SS is also fairly similar between the ANL results. This demonstrates that the RELAP model is capable of reasonably reproducing the CFD results for this class of transient.

Table 6. Initial and final temperatures for the step transient. ANL CFD results here are surface (not volume) averages.

	IAE CFD twisted	ANL CFD cylindrical	ANL CFD twisted	ANL RELAP cylindrical (10 mm-node case)
Initial Clad Temp., 0.1m [K]	316.3	316.4	316.3	316.8
Final Clad Temp., 0.1m [K]	318.3	318.5	318.3	319.0
Initial Fluid Outlet Temp. [K]	315.8	315.9	315.9	315.9
Final Fluid Outlet Temp. [K]	317.8	317.8	317.8	317.8
Time to Reach Steady-State, Coolant Outlet (s)	1.0	1.2	1.3	1.2

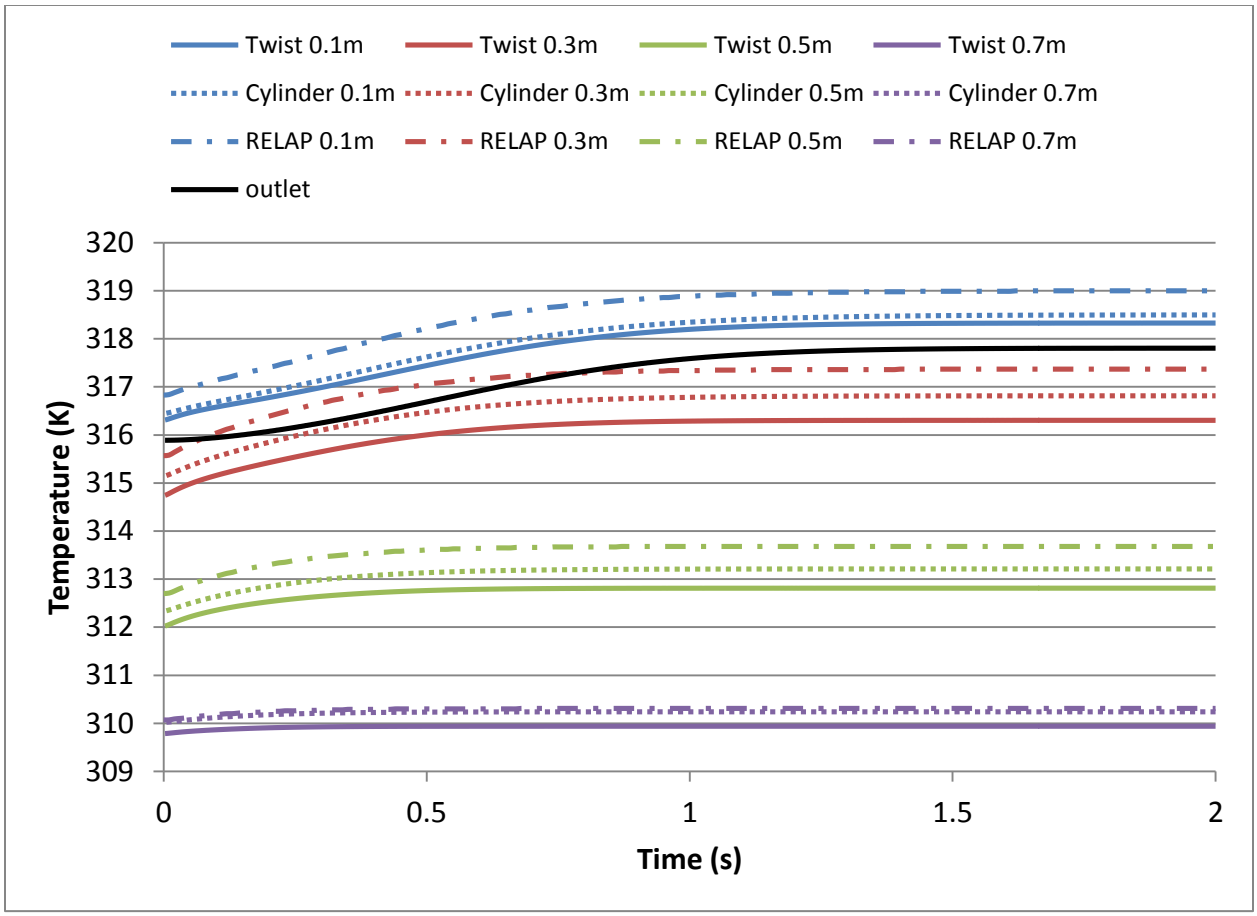

Fig. 32. Temperature plots of cladding surface temperature averages at various axial locations for CFD twisted (solid), CFD cylindrical (dotted), and RELAP (dot-dash). Coolant outlet temperature is also plotted and was similar between the codes.

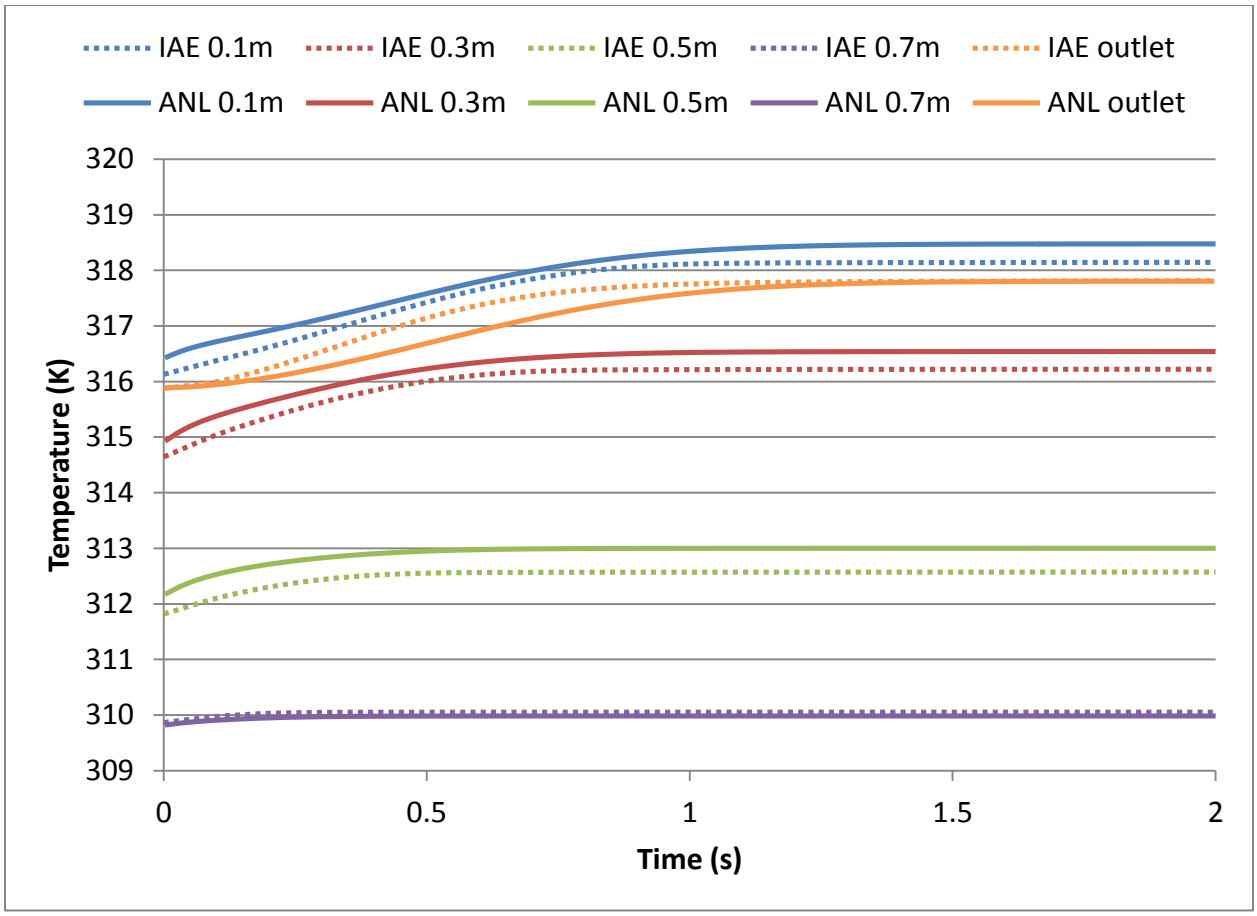

Fig. 33. Comparison of coolant outlet and cladding volume-averaged temperatures at various axial locations between the ANL (solid) and IAE (dotted) twisted pin CFD models. Each location is in agreement within 0.5 K.

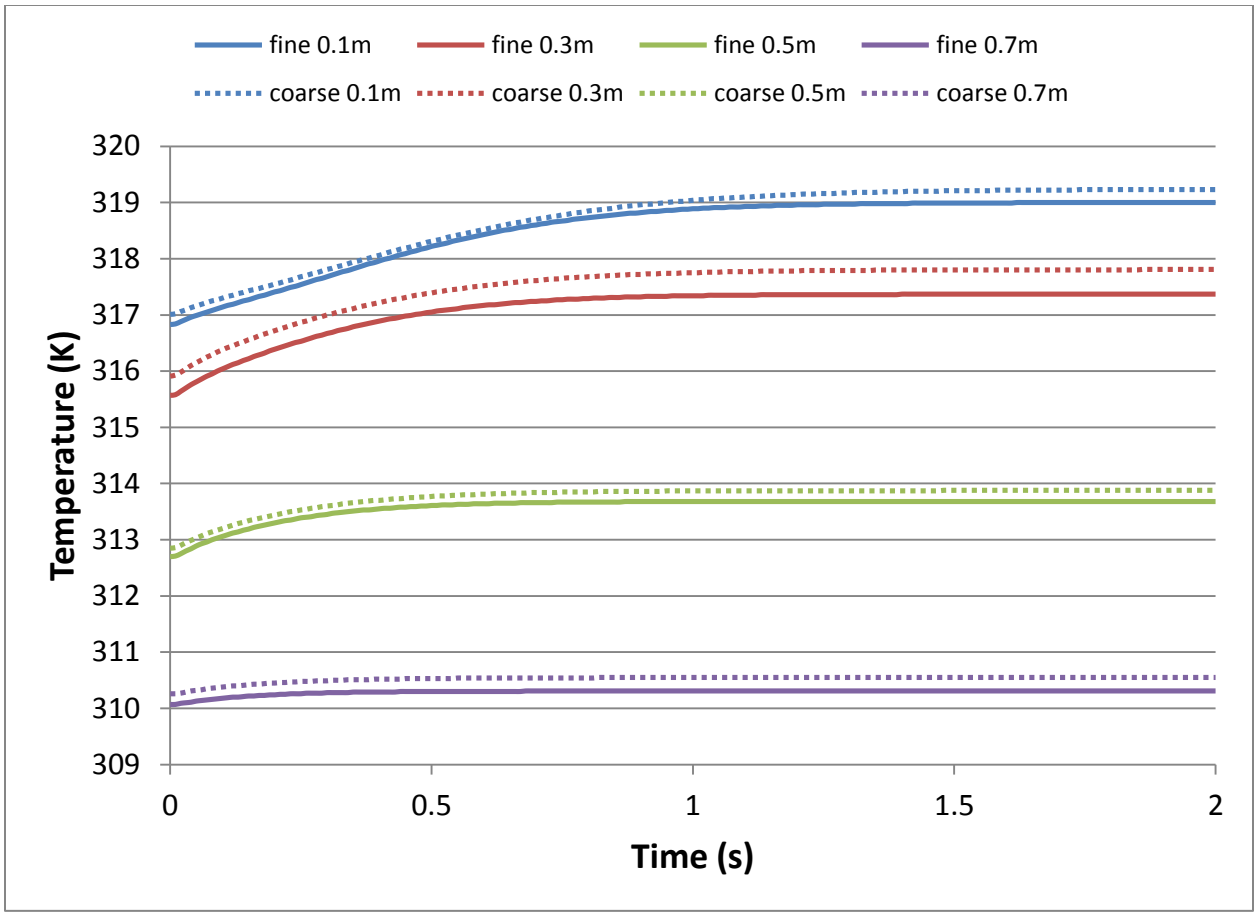

Fig. 34. Comparison of fine (solid) vs. coarse (dotted) nodalizations in RELAP.

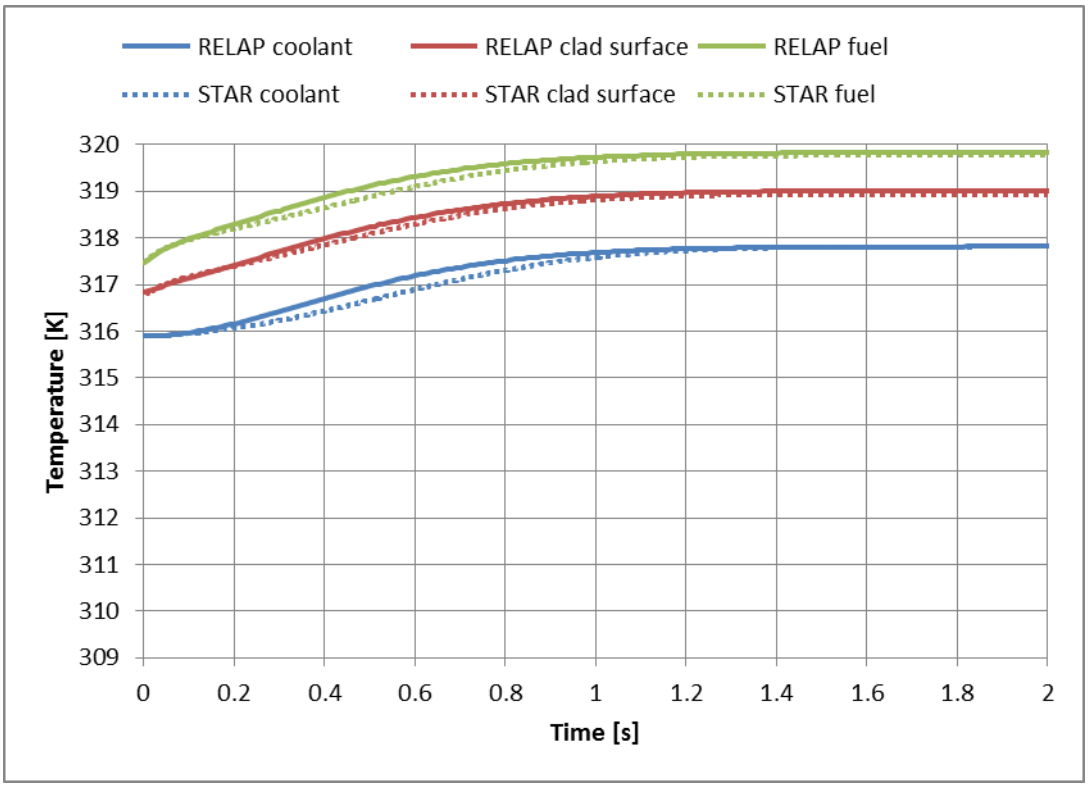

Fig. 35. Peak temperature comparison for RELAP and ANL CFD twisted models.

While the ANL CFD and RELAP models produce rather similar results, these results have some notable differences as compared to the IAE values. The initial temperatures for the transient are marginally different, indicating that there is some difference between the models at the SS level. A much larger disparity is found in the time to reach the new SS, particularly noticeable for the coolant outlet. The ANL cases all reach SS much slower than the IAE case (Table 6). Since the ANL results are largely consistent, this suggests that there is some fundamental difference between the modeling approaches of ANL and IAE. This difference is being investigated further.

It is important to realize, however, that the goal of the "fast" scenario was to use the IAE transient as "inspiration" in order to have more varied test cases for justification of using the current RELAP approach for realistic transients. This goal was successfully realized. Explicitly matching the IAE results was not the primary goal at this stage, as a number of details of the IAE simulation approach were not available which could have led to discrepancies. These include mesh density, time step size, solution order, turbulence model, power shape interpolation, and so forth. Once these details are known and evaluated, a more thorough comparison of the IAE and ANL approaches would be more appropriate. This should help bolster the accuracy of the approach for dynamic simulations.

V. CONCLUSIONS

In summary, the steady-state properties of the peak power assemblies have been characterized for one possible configuration of the IVG.1M reactor at the 10MW power level. The peak temperatures for the cladding surface have sufficient margin to the boiling point at the rated pressure, and the peak fuel temperature is far below melting. Parametric studies on various simplifications, such as straight-pin approximations and pin orientations, do not show strong variability in temperature predictions.

The results have shown, as hoped, that the single-pin approximation is generally valid and conservative when based on the average flow rate and peak power. The twisted pin has the advantage of incorporating more realistic flow physics. Thus this approximation can likely be used to evaluate future cases much more quickly. Further work may include parametric studies on the pin and filler positions and the manufacturing tolerances, as well as potential LEU core designs.

The transients investigated in this work tested fast and slow power increases, as well as two different core powers and inlet temperatures. In each case, RELAP showed reasonable agreement with CFD. This provides some validation that the heat transfer coefficients and other parameters chosen for RELAP can be used more confidently for safety analysis of realistic transients for IVG. Future transient work may include more in-depth comparisons of the ANL and IAE CFD models for further transients.

VI. ACKNOWLEDGMENTS

The authors would like to thank Elia Merzari and Paul Fischer for performing the Nek5000 simulations and for their insights regarding the problem physics.

VII. REFERENCES

1. A. D. Vurim, A. N. Kolbaenkov, V. S. Gnyrya, “Description of Reactor IVG.1M”, Deliverable 2.1 under ANL-IAE Work Order 0J-30461-0002, Institute of Atomic Energy, Kurchatov, Kazakhstan (November 2010).

2. Personal Communication, Institute of Atomic Energy, Kurchatov, Kazakhstan.

3. A.A. Kolodeshnikov, A.D. Vurim, V.A. Zuev, “HEU Core Characterization of IVG.1M Reactor”, Deliverable 2.2 under ANL-IAE Work Order 0J-30461-0002, Institute of Atomic Energy, Kurchatov, Kazakhstan (December 2011).

4. “User Guide, STAR-CCM+ Version 8.04,” CD-Adapco, Melville, NY, 2013.

5. E.W. Lemmon, M.O. McLinden and D.G. Friend, "Thermophysical Properties of Fluid Systems" in NIST Chemistry WebBook, NIST Standard Reference Database Number 69, Eds. P.J. Linstrom and W.G. Mallard, National Institute of Standards and Technology, Gaithersburg MD, 20899, http://webbook.nist.gov.

6. Paul F. Fischer, James W. Lottes and Stefan G. Kerkemeier, "Nek5000 Web Page", http://nek5000.mcs.anl.gov.

7. Adam R. Kraus, Elia Merzari and Paul F. Fischer, "Turbulent Flow-Field Comparisons of RANS and LES for a Twisted Pin Lattice Geometry at Low Reynolds Number", *Proceedings of the ASME 2014 4th Joint US-European Fluids Engineering Division Summer Meeting and 11th International Conference on Nanochannels, Microchannels, and Minichannels* (FEDSM2014, Chicago, USA, August 3-7, 2014).

8. RELAP5-3D Code Manual, INEEL-EXT-98-00834, Idaho National Laboratory, Idaho Falls, Idaho, USA (June 2012).

9. A. D. Vurim, A. A. Kolodeshnikov, V. S. Gnyrya (and others), "Develop Kinetics Code", Deliverable 10.2 under ANL-IAE Work Order 0J-30461-0010, Institute of Atomic Energy, Kurchatov, Kazakhstan (Draft May 2014).

Nuclear Engineering Division
Argonne National Laboratory
9700 South Cass Avenue, Bldg. 208
Argonne, IL 60439

www.anl.gov

Argonne National Laboratory is a U.S. Department of Energy
laboratory managed by UChicago Argonne, LLC